

Galaxies at $z = 6 - 9$ from the WFC3/IR imaging of the HUDF

R. J. McLure^{1*}, J. S. Dunlop¹, M. Cirasuolo^{1,2}, A. M. Koekemoer³, E. Sabbi³,
D. P. Stark⁴, T. A. Targett⁵, R.S. Ellis⁶

¹ SUPA†, Institute for Astronomy, University of Edinburgh, Royal Observatory, Edinburgh, EH9 3HJ, UK

² UK Astronomical Technology Centre, Royal Observatory, Edinburgh, EH9 3HJ, UK

³ Space Telescope Science Institute, 3700 San Martin Drive, Baltimore, MD 21218, USA

⁴ Kavli Institute of Cosmology, University of Cambridge, Madingley Road, Cambridge, CB3 0HA, UK

⁵ Department of Physics & Astronomy, University of British Columbia, 6224 Agricultural Road, Vancouver, BC V6T 1Z1, Canada

⁶ Department of Astronomy, California Institute of Technology, Pasadena, CA 91125, USA

Accepted ... ; Received ... ; in original form ...

ABSTRACT

We present the results of a systematic search for galaxies in the redshift range $z = 6-9$, within the new, deep, near-infrared (Y, J, H) imaging of the Hubble Ultra Deep Field provided by the Wide Field Camera 3 (WFC3) on the Hubble Space Telescope. We have performed full spectral energy distribution fitting to the optical+infrared photometry of all high-redshift galaxy candidates detected at $\geq 5\sigma$ significance in at least one of the WFC3/IR broad-band filters. After careful rejection of contaminants, the result is a sample of 49 galaxies with primary photometric redshift solutions $z > 5.9$, within the 4.5 arcmin² field covered by the new near-infrared imaging. Our sample, selected without recourse to specific colour cuts, re-selects all but the faintest one of the 16 z_{850} -drops selected by Oesch et al. (2009), recovers all 5 of the Y_{105} -drops reported by Bouwens et al. (2009), and adds a further 29 equally plausible galaxy candidates, of which 12 lie beyond $z \simeq 6.3$, and 4 lie beyond $z \simeq 7.0$. However, we also present confidence intervals on our photometric redshift estimates, including alternative secondary redshift solutions. As a result of this analysis we caution that acceptable low-redshift ($z < 2$) solutions exist for 28 out of the 37 galaxies at $z > 6.3$, and in particular for all 8 of the galaxy candidates reported here at $z > 7.5$. Nevertheless, we note that the very highest redshift candidates appear to be strongly clustered in the field. Based on our photometric redshift analysis we derive new estimates of the ultraviolet galaxy luminosity function at $z \simeq 7$ and $z \simeq 8$. Where our results are most robust, at a characteristic luminosity $M_{1500} \simeq -19.5(AB)$, we find that the comoving number density of galaxies declines by a factor of $\simeq 2.5$ between $z \simeq 6$ and $z \simeq 7$, and by a further factor of $\simeq 2$ by $z \simeq 8$. These results suggest that it is difficult for the observed population of high-redshift star-forming galaxies to achieve reionisation by $z \simeq 6$ without a significant contribution from galaxies well below the detection limits, plus alterations in the escape fraction of ionising photons and/or continued vigorous star formation at $z > 15$.

Key words: cosmology: observations - galaxies: evolution - galaxies: formation - galaxies: high-redshift

1 INTRODUCTION

A key goal of modern observational cosmology is to discover and study the first galaxies, and to quantify their role in the reionisation of the neutral universe at redshifts $z > 7$ (Dunkley et al., 2009). Studies of quasars have now reached beyond $z \simeq 6$ (e.g. Fan et al. 2006) and indicate that the Gunn-Peterson (1965) optical depth due to neutral hydrogen in the intergalactic medium (IGM) increases

significantly at these redshifts. Whatever the precise implications for reionisation physics, the increased strength of the Lyman-break produced by this enhanced optical depth should make it relatively straightforward to select still higher-redshift objects via the Lyman-break technique (e.g. Steidel et al. 1996), given sufficiently sensitive broad-band imaging.

Over recent years, galaxy evolution studies have indeed been successfully extended to redshifts $z > 6$, via both ground-based and *Hubble Space Telescope* (HST) searches for objects with either strong Lyman breaks and/or strong Lyman- α emission at observed wavelengths $\lambda_{obs} > 8500\text{\AA}$ (e.g. Bouwens et al. 2004; Yan

* Email: rjm@roe.ac.uk

† Scottish Universities Physics Alliance

& Windhorst 2004; Stark et al., 2007; Bouwens et al. 2008; Richard et al. 2008; McLure et al. 2009; Oesch et al. 2009a; Zheng et al. 2009; Ouchi et al. 2009). However, it has proved very difficult to push the discovery space beyond $z \simeq 7$. The highest spectroscopically confirmed redshift is $z = 6.96$ (Iye et al. 2006), and there currently exist at most 2 or 3 convincing candidates at redshifts just greater than $z = 7$ (Bouwens et al. 2008; Bradley et al. 2008; Richard et al. 2008; Oesch et al. 2009a; see Section 2). This current redshift “limit” is almost certainly in part due to continued (potentially steepening) decline in the number density of galaxies at higher redshifts, as anticipated from the negative evolution of the galaxy luminosity function found between $z = 4$ and $z = 6$ (Bouwens et al. 2006; McLure et al. 2009). However, action is clearly required at higher redshifts to commence and maintain reionisation, and extensive star-formation at $z > 7$ is implied by the stellar masses of galaxies at $z \simeq 6$ (Stark et al. 2009) and by reports of Balmer breaks in their spectral energy distributions (SEDs) (Eyles et al. 2007). Most recently, spectacular direct evidence of action at $z > 8$ has been provided by the discovery of a gamma ray burst at $z \simeq 8.2$ (Tanvir et al. 2009; Salvaterra et al. 2009). Consequently the most likely reason for the current galaxy redshift limit of $z \simeq 7$ is a practical one, namely that the convincing discovery of galaxies at higher redshifts requires more sensitive near-infrared imaging than has been available until now. Specifically, to uncover a galaxy at $z \simeq 8$ on the basis of a strong Lyman break at $\lambda_{rest} = 1215\text{\AA}$ requires deep imaging at $\lambda_{obs} > 1.1\mu\text{m}$ in at least 2 filters (to establish the existence of a blue continuum longward of the break), *and* imaging at $\lambda_{obs} \simeq 0.9 - 1.1\mu\text{m}$ of sufficient depth for a non-detection to provide convincing evidence of a sharp Lyman break in the spectrum. The recent installation of Wide Field Camera 3 (WFC3) on the HST offers the first realistic opportunity to achieve the required multi-filter near-infrared sensitivity levels over significant areas of sky. In this study we use the first deep imaging from this revolutionary new instrument to extend the study of galaxy evolution into the crucial reionisation epoch corresponding to $z = 7 - 10$ (Dunkley et al. 2009).

The specific aim of the work presented here is to use the first release of deep HST WFC3/IR imaging in the Hubble Ultra Deep Field (HUDF; Beckwith et al. 2006), in tandem with the existing HST Advanced Camera for Surveys (ACS) optical imaging to select and study a new sample of galaxies at $z > 6$, with the expectation that this new sample could extend to $z > 8$ (due to the extreme depth of the new near-infrared imaging – see Section 3).

The paper is structured as follows. In Section 2 we summarize what is currently known about high-redshift galaxies in the HUDF, based on the handful of potential $z > 6.5$ galaxy candidates selected using the existing HST NICMOS+ACS dataset. The new WFC3/IR data are described in Section 3, where we summarize the key properties of the new WFC3/IR instrument, discuss the observing strategy of the HST HUDF09 Treasury programme, and explain how we reduced the raw near-infrared imaging data after public release on September 9, 2009. Next, in Section 4, we describe how we selected and refined our high-redshift galaxy catalogue from the combined WFC3/IR+ACS+Spitzer imaging data now available in the field. We also explain how we used SED fitting to derive photometric redshifts (with confidence intervals) for all plausible high-redshift galaxy candidates, and used this information to clean the sample for a range of contaminants. In Section 5 we present and discuss the final sample of galaxies in the redshift range $z = 6 - 8.5$, explore the robustness and implications of the new very high-redshift sub-sample, derive a first meaningful estimate of the evolution of the galaxy luminosity function out to

RA(J2000)	Dec(J2000)	Bouwens et al. 04/08	Oesch et al. 09a
03 02 38.80	−27 47 07.2	UDF-983-964	HUDF-480
03 32 44.02	−27 47 27.3	UDF-3244-4727	HUDF-708
03 32 42.56	−27 46 56.6	UDF-640-1417	
03 32 42.56	−27 47 31.4	UDF-387-1125	
03 32 39.54	−27 47 17.4	UDF-825-950	

Table 1. Existing galaxy candidates at $z > 6.5$ in the HUDF as derived from the NICMOS+ACS imaging available in the field since 2004. Five candidates have survived, two of which plausibly lie at $z > 7$ (see Fig. 1). As well as positions, catalogue numbers as used by Bouwens et al. (2004,2008) and by Oesch et al. (2009a) are given for ease of reference. All except the second of these candidates have been re-imaged in the current programme with WFC3, and survive in our final high-redshift galaxy sample presented in Table 2.

$z \simeq 8$, and briefly explore the implications for our understanding of cosmic reionisation. Finally, we summarize our conclusions in Section 6.

We give all magnitudes in the AB system (Oke & Gunn 1983), and for cosmological calculations assume $\Omega_0 = 0.3$, $\Omega_\Lambda = 0.7$, and $H_0 = 70 \text{ km s}^{-1} \text{ Mpc}^{-1}$.

2 EXISTING REDSHIFT 7 GALAXY CANDIDATES IN THE HUDF

The first study to claim to have isolated galaxies at “ $z \simeq 7-8$ ” was that of Bouwens et al. (2004), who reported 6 z_{850} -drops derived from the combined NICMOS J_{110} , H_{160} and ACS z_{850} imaging of the HUDF. Bouwens et al. (2004) suspected that two of their candidates were possibly not real (UDF-491-880, and UDF-818-886), due to the fact they were not found in an independent reduction of the NICMOS imaging undertaken by Massimo Robberto. This scepticism was justified, as neither of these objects is seen in the new, deeper WFC3/IR imaging. Subsequently, Bouwens et al. (2008) added a fifth plausible candidate. This, plus one of the original 4 candidates, was also identified as a high-redshift candidate in an independent study by Oesch et al. (2009a).

The positions of these 5 surviving NICMOS-selected $z \simeq 7$ galaxy candidates, along with their pre-existing alternative catalogue names, are summarized in Table 1. Our own analysis of the NICMOS+ACS photometry for these objects in fact indicates that only the first two objects listed in Table 1 (i.e. the two galaxies confirmed by Oesch et al. 2009a) actually lie at $z > 7$, and SED fits and redshift constraints on these two galaxies are illustrated in Fig. 1 (see Section 4.2 for details of the SED fitting procedure).

Unfortunately UDF-3244-4727 (= HUDF-708) has been missed by the pointing chosen for the new WFC3/IR image within the HUDF (see Section 3.3). However, the reality of the other 4 candidates listed in Table 1 has been confirmed by the new WFC3 imaging, and we present revised redshift estimates for these objects (based on the vastly improved photometry) in Section 4 alongside the results for the new high-redshift galaxy candidates.

3 NEW HST WFC3/IR DATA

3.1 Wide Field Camera 3

Wide Field Camera 3 (WFC3) is the new near-infrared (WFC3/IR) and optical/ultra-violet (WFC3/UVIS) camera onboard the refur-

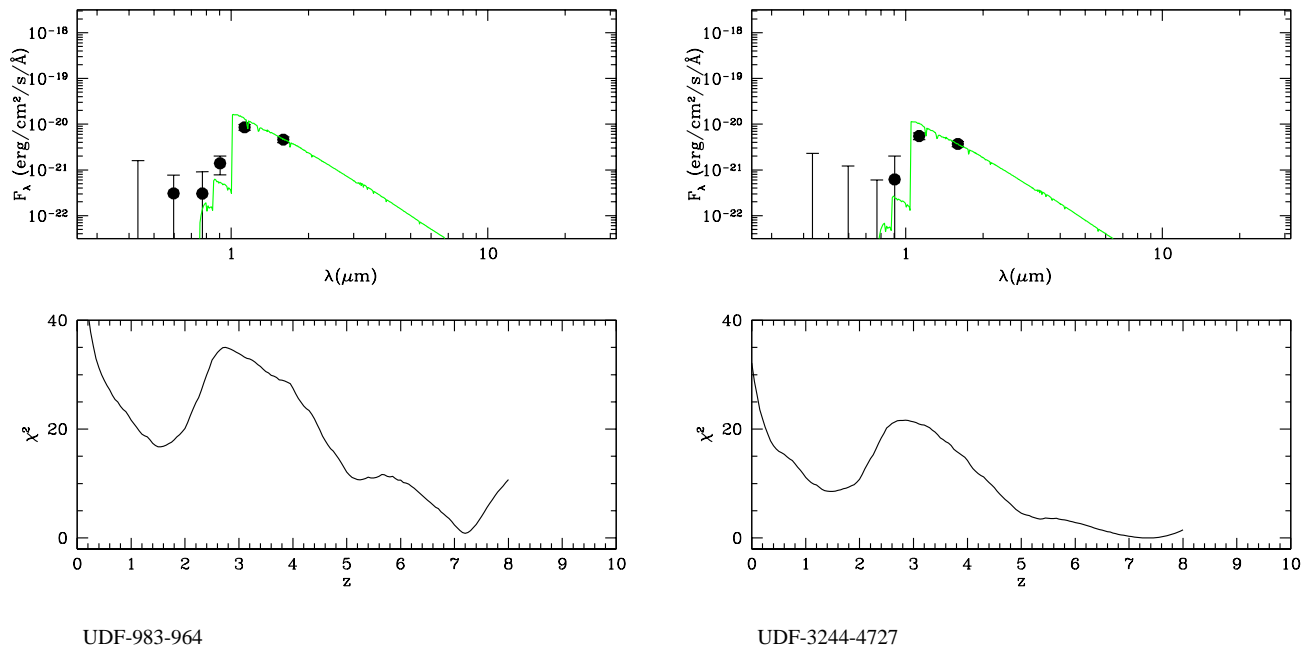


Figure 1. The results of our SED fitting to the optical (ACS) and near-infrared (NICMOS F110W & F160W) photometry for the two most plausible galaxy candidates at $z > 7$ discovered within the HUDF prior to the new WFC3/IR imaging campaign. The upper panels show the best-fitting SED while the lower panels show the dependence of χ^2 on redshift (marginalised over all other fitted parameters).

bished HST. The detector on the near-infrared channel is a 1024×1024 HgCdTe array, in which the semi-conductor band-gap has been enhanced to produce a sharp drop in sensitivity beyond $\lambda = 1.7 \mu\text{m}$. 1014×1014 pixels are exposed to the sky (the remainder providing reference pixels to track bias drifts), and the resulting field of view is 123×136 arcsec, with a pixel scale of 0.13 arcsec.

WFC3/IR is equipped with 17 filters. The filters used in the present study are the wide filters F105W (Y_{105}), F125W (J_{125}), and F160W (H_{160}), with these 3 bands being selected as most appropriate for providing sufficient depth *and* also sufficient colour information to successfully isolate high-redshift galaxies (i.e. although F105W and F125W do overlap somewhat, in combination they offer much better redshift discrimination than F110W, the even wider $Y + J$ filter previously used in deep NICMOS imaging).

The WFC3/IR instrument represents a major advance over the NICMOS camera. Its field of view is $\simeq 6$ times greater, it is 2 – 4 times as sensitive, and it offers a $\simeq 2$ times improvement in angular resolution. For a programme that aims to conduct a blank-field search for faint, compact, objects, these improvements add up to a factor of $\simeq 30 - 40$ improvement in survey efficiency.

3.2 Observing Programme

This study utilises new deep Y_{105} , J_{125} and H_{160} imaging taken with a single $\simeq 4.5$ arcmin² pointing of WFC3/IR within the wider 11 arcmin² covered by the existing HST ACS optical imaging of the HUDF. This is one of 3 ultra-deep WFC3/IR pointings which will be completed over the next year (the other two will be located within the nearby HUDF05 parallel fields; Oesch et al. 2007) as part of the 192-orbit HUDF09 HST Treasury programme GO-11563 (P.I. G. Illingworth).

The first 62 orbits of observations in the HUDF were obtained

from August 26, 2009 to September 6, 2009, with the raw data being released to the public on September 9, 2009.

3.3 Field selection and supporting data

The WFC3/IR pointing in the HUDF is centred on $3^{\text{h}}32^{\text{m}}38.5^{\text{s}}$, $-27^{\circ}47'0.0''$. As shown in Fig. 2, this pointing lies somewhat to the north of the existing NICMOS F110W and F160W imaging within the HUDF (Thompson et al. 2005), and the deep VLT ISAAC K' -band image referred to by Labbe et al. (2006) (which reaches a 5σ detection limit of $K'(AB) \simeq 25.5$).

The WFC3/IR pointing still lies within the ACS image, and thus benefits from the ultra-deep, high-resolution, optical data obtained by HST in 4 different filters: F_{435W} (B_{435}), F_{606W} (V_{606}), F_{775W} (i_{775}) and F_{850LP} (z_{850}) (Beckwith et al. 2006). These deep optical data (in particular the 150 orbits of z_{850} imaging) are crucial for the effective exploitation of the new deep WFC3/IR data in the search for galaxies at $z > 7$, where the fundamental aim is to establish the existence of a strong Lyman break ($\lambda_{rest} = 1215\text{\AA}$) redshifted to $\lambda_{obs} > 9500\text{\AA}$. Within a 0.6 arcsec diameter aperture, we find these optical data reach 5σ detection limits of $B_{435} = 28.8$, $V_{606} = 29.2$, $i_{775} = 28.8$, $z_{850} = 28.1$ (consistent with the smaller aperture depths quoted by Bouwens et al. 2006).

Finally, the HUDF is also covered by ultra-deep *Spitzer* imaging with the Infrared Array Camera (IRAC: Fazio et al. 2004) taken as part of GOODS (proposal ID 194, Dickinson et al., in preparation), in all 4 IRAC channels (3.6, 4.5, 5.6, and $8.0\mu\text{m}$). The IRAC 5σ (AB mag) detection limits are $S_{3.6} \simeq 25.9$, $S_{4.5} \simeq 25.5$, $S_{5.6} \simeq 23.3$, $S_{8.0} \simeq 22.9$.

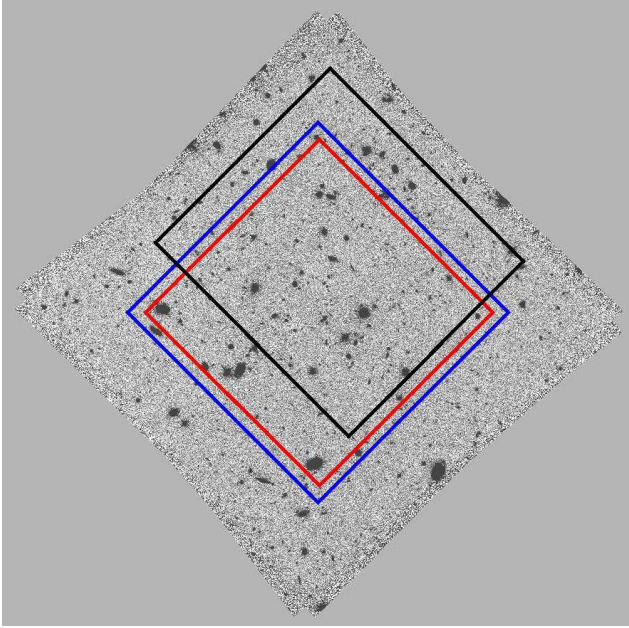


Figure 2. The new WFC3 pointing is indicated by the black rectangle superimposed on the HST ACS z_{850} image of the HUDF. The blue box shows the location of the existing HST NICMOS F110W and F160W imaging of the field (Thompson et al. 2005), while the red box indicates the region covered by the deep K' -band image obtained with ISAAC on the VLT (Labbé et al. 2006).

3.4 Data acquired

The new HST near-infrared data were obtained over a total of 31 2-orbit visits with 2 WFC3/IR exposures being taken in each orbit. The total of 62 orbits was divided into 28 orbits in H_{160} , 16 orbits in J_{125} , and 18 orbits in Y_{105} . Unfortunately, the Y_{105} -band exposures in two orbits were significantly affected by persistence from bright sources in an unrelated HST observing programme, and were excluded from subsequent image combination.

All exposures had the same integration time of 1400 seconds and were obtained in MULTIACCUM mode using the SPARS100 readout sequence, which involves a series of non-destructive samples of the detector at equally spaced intervals of 100 seconds. An additional pair of reads was obtained at the start of each exposure, with the first read effectively serving as the bias level for the remainder of the exposures. Small (< 1 arcsec) offsets were made between each of the four 1400-second exposures in a given visit. Larger offsets, of up to 10 arcsec, were made between different visits.

3.5 Data reduction

The exposures were calibrated using the latest version of the STS-DAS Pyraf task calwfc3 (released on September 9, 2009) which applies bias level removal using the zero-th read of each exposure, as well as dark current subtraction, flat-fielding and linearity correction. Since the standard pipeline calibration was based on ground-based dark current and flat-field files, a new “superdark” file was constructed from on-orbit dark exposures obtained during approximately the same time frame as the observations, and which became public at the same time. Comparison tests were carried out between the calibration results of the pipeline ground-based darks and the

new on-orbit darks, showing that the latter resulted in improved dark current subtraction of the exposures.

Remaining low-level residuals in the images were removed iteratively, after first combining the images using MultiDrizzle (Koekemoer et al. 2002) which makes use of the drizzle software (Fruchter & Hook 2002). This allowed us to create a clean image of the field which could then be used to create a high signal-to-noise source mask. This source mask was then transformed back to the frame of each detector, and a large-scale, low-resolution median filter was applied to the remaining pixels in order to create an image characterizing the low-order residuals for each filter. This process also involved treating the four amplifier quadrants separately, in order to include differences between the amplifiers in the low-level residual image. When running MultiDrizzle, the images were combined using inverse variance weighting, which involves calculating for each exposure the total expected noise due to the background sky (modulated by the flatfield structure), as well as the accumulated dark current and read noise added in quadrature, giving the total noise component due to the background. This is compared with the final r.m.s. in the multidrizzled images, in order to assess the amount of correlated noise in the final images.

After applying the scaled residual image correction to each exposure, the exposures were verified to have no significant remaining residual signature and were combined using MultiDrizzle (Koekemoer et al. 2002), this time creating a new drizzled image for each of the 3 filters, with no significant low-level residuals remaining. The output scale was set to 0.03 arcsec per pixel in order to match the original ACS images; a total of 850 - 900 sources were matched between the WFC3 and ACS images in order to determine the astrometric solution and geometric transformation from the WFC3 to the original UDF ACS images, which were taken as the astrometric reference frame. The resulting astrometric solutions were applied to the image header world coordinate system parameters and distortion coefficients for each exposure, and MultiDrizzle was then re-run to create images at both 0.03-arcsec and 0.06-arcsec per pixel, matched to the ACS astrometry.

The resulting images are aligned to the ACS data with an r.m.s. of $\simeq 0.1$ times the final WFC3 PSF and are on the same pixel grid as the ACS images, enabling direct photometry to be carried out between the datasets. A pixfrac of 0.6 was used to minimize additional convolution; the small output pixel size also reduces the convolution of the PSF, with the resulting PSF widths being 0.15 arcsec in Y_{105} , 0.16 arcsec in J_{125} , and 0.18 arcsec in H_{160} , matching the theoretical values expected after convolution by the 0.13-arcsec WFC3/IR pixels is taken into account.

The final WFC3/IR images have total exposure times of $\simeq 11$ hours in Y_{105} , $\simeq 12$ hours in J_{125} , and $\simeq 22$ hours in H_{160} .

3.6 Photometric Zero Points

We established our own independent zero points by comparison with catalogues derived from deep ground-based imaging of the field in the Y -band with VLT+HAWK-I (Programme ID: 60.A-9284(A)) and in the J - and H -bands with VLT+ISAAC (Programme ID: 168.A-0485). Moreover, we also independently checked our H -band zero point determination using objects in the overlap region between the new WFC3 imaging and the existing deep NICMOS F160W imaging of the HUDF (Thompson et al. 2005). Finally, we confirmed our zero point determination using large aperture (6-arcsec diameter) photometry of two bright stars in the HUDF which were found to have approximately flat $Y - H$ colours from the existing ground-based imaging. This pro-

cess led to the determination of the following AB zero points: $Y_{105}(zpt) = 26.25$, $J_{125}(zpt) = 26.25$ and $H_{160}(zpt) = 26.00$, with a typical uncertainty of $\simeq 0.05$ magnitudes. We note here that our independent determinations of the Y_{105} , J_{125} and H_{160} –band zero points are within 0.04 magnitudes of the most recent, on-orbit values¹.

Following the determination of the photometric zero points we derived robust measurements of the image depths in the three near-infrared bands. To achieve this we placed a grid of $\geq 10,000$ circular apertures on blank sky regions within the final WFC3/IR mosaics. The resulting distribution of blank sky aperture fluxes was then used to determine the r.m.s. background noise of the WFC3/IR mosaics on the scale of our chosen apertures. In order to determine what regions of the images were largely uncontaminated by object flux we used a χ^2 image (Szalay et al. 1999) constructed from the deep *BViz* ACS imaging of the HUDF. The results of this analysis demonstrated that, within 0.4-arcsec diameter apertures, the 5σ depths of our reductions of the WFC3 images are $Y_{105} = 29.01$, $J_{125} = 29.07$ and $H_{160} = 29.08$ (we note that this is consistent with the approximate 5σ depth of $\simeq 29$ in all bands derived from their own independent reduction by Bouwens et al. 2009).

4 THE HIGH-REDSHIFT GALAXY SAMPLE

4.1 Catalogue extraction and photometry

The original master object catalogue for this study was produced using version 2.5.2 of the SExtractor software package (Bertin & Arnouts 1996). For this catalogue we included all objects which were detected at $\geq 5\sigma$ significance in at least one of the near-infrared images in a 0.4-arcsec diameter aperture. For the purposes of SED analysis and photometric redshift determination we performed aperture photometry on all objects within circular apertures of 0.6-arcsec diameter. This aperture encloses $\simeq 80\%$ of the total flux of a point source in all three WFC3 images and has a consistent point-source aperture correction of 0.22 ± 0.03 magnitudes from Y_{150} through to H_{160} . Moreover, the choice of 0.6-arcsec diameter apertures avoids biases which can result from very small aperture photometry, the use of which implicitly assumes that high-redshift galaxies are unresolved (and inspection of the images shows that a substantial fraction of the high-redshift galaxy candidates are resolved by WFC3).

Starting from the master catalogue we confined our attention to high redshifts by rejecting all sources which were detected at $\geq 2\sigma$ significance in the ACS *i*–band imaging of the UDF. This resulted in a sample of $\simeq 300$ objects which, while incomplete for *i*-drops, should retain all potential *i*-dropouts and higher-redshift galaxy candidates at $z > 6.25$.

To homogenise the photometry, and to avoid confusion over how to aperture-correct upper limits on non-detected sources, we corrected the WFC3/IR 0.6-arcsec diameter magnitudes for missing point-source flux density *relative* to the ACS optical imaging. These corrections were determined empirically from point sources in the field (common to all images) and amount to corrections of 0.02, 0.04 and 0.08 mag in Y_{105} , J_{125} and H_{160} respectively.

4.2 Redshift estimation

In contrast to Oesch et al. (2009b) and Bouwens et al. (2009) we have not used 3-band colour information to attempt to select high-redshift galaxies in different redshift windows. Rather we performed a full SED fit to the 7-band photometry for all $\simeq 300$ candidates to derive estimates of, and constraints on their redshifts. Inspection of the available IRAC data shows that none of our high-redshift candidates are securely detected at $\geq 2\sigma$ significance in the $3.6\mu\text{m}$ and $4.5\mu\text{m}$ imaging (c.f. Labbé et al. 2009). However, due to the lack of comparably deep near-imaging at wavelengths longer than $1.6\mu\text{m}$ (e.g. *K*-band) it is important to make use of the information provided by the IRAC non-detections to help rule-out otherwise acceptable redshift solutions at $z \simeq 5 - 6$. Consequently, during the SED fitting procedure we adopted 2σ upper limits for the non-detections at $3.6\mu\text{m}$ and $4.5\mu\text{m}$ of 26.0 (AB), which are a factor of $\simeq 2$ brighter than the recent determination by Labbé et al. (2009). We note that this is a conservative approach, and that a robust de-confusion of the available IRAC data (Cirasuolo et al. 2010, in prep) is expected to produce 2σ limits which are fainter, and therefore more able to rule-out potential $z \simeq 5 - 6$ solutions. Moreover, as in Dunlop et al. (2007), rather than simply adopting global upper limits for non-detections in the optical/near-infrared wavebands, we have retained even low-significance measurements of flux-density and derived the locally measured r.m.s. within a series of 0.6-arcsec diameter apertures for use in the SED fitting process.

The SED fitting procedure we applied to derive the photometric redshifts of the high-redshift galaxy candidates was based largely on the public package Hyperz (Bolzonella et al. 2000). The observed photometry was fitted with synthetic galaxy templates generated with the 2007 stellar population models of Charlot & Bruzual. We used a variety of star-formation histories: instantaneous burst and exponentially declining star-formation with e-folding times $0.1 \leq \tau(\text{Gyr}) \leq 10$, assuming solar metallicity and a Salpeter initial mass function (IMF). At each redshift step we allowed galaxy templates with ages ranging from 1 Myr to the age of the Universe at that redshift. Moreover, in addition to the synthetic stellar populations we also used the composite SED of Lyman-break galaxies at $z \simeq 3$ derived by Shapley et al. (2003). For dust reddening we adopted the prescription from Calzetti et al. (2000), within the range $0 \leq A_V \leq 2$, and included absorption due to H_I clouds along the line of sight according to Madau (1995).

Examination of the resulting SED fits and plots of χ^2 versus z then allowed us to reject sources with no acceptable redshift solutions at $z > 6$, and identify “objects” with peculiar SEDs which we then confirmed visually to be artefacts (e.g. the result of diffraction spikes) or objects for which the photometry was compromised by confusion with nearby galaxies. As shown in the left-hand panel of Fig. 3, our χ^2 versus z plots also helped us to notice a peculiarly bright and unusually secure high-redshift object, which we then noticed was highly stellar, and revealed itself to be a supernova or other transient interloper due to its complete absence in the pre-existing NICMOS infrared images of the UDF. Moreover, in the right-hand panel of Fig 3 we show our SED fit to UDFz-38537519, the faintest $z \simeq 7$ galaxy reported by Oesch et al. (2009b). Adopting 2σ upper limits for its non-detection in z_{850} , this object is very close to the edge of the two-colour selection box employed by Oesch et al. (2009b), and our SED fitting analysis suggests that it is most likely a low-mass interloper at $z \simeq 1.5$. This object illustrates the advantage of full SED fitting when dealing with objects close

¹ <http://www.stsci.edu/hst/wfc3>

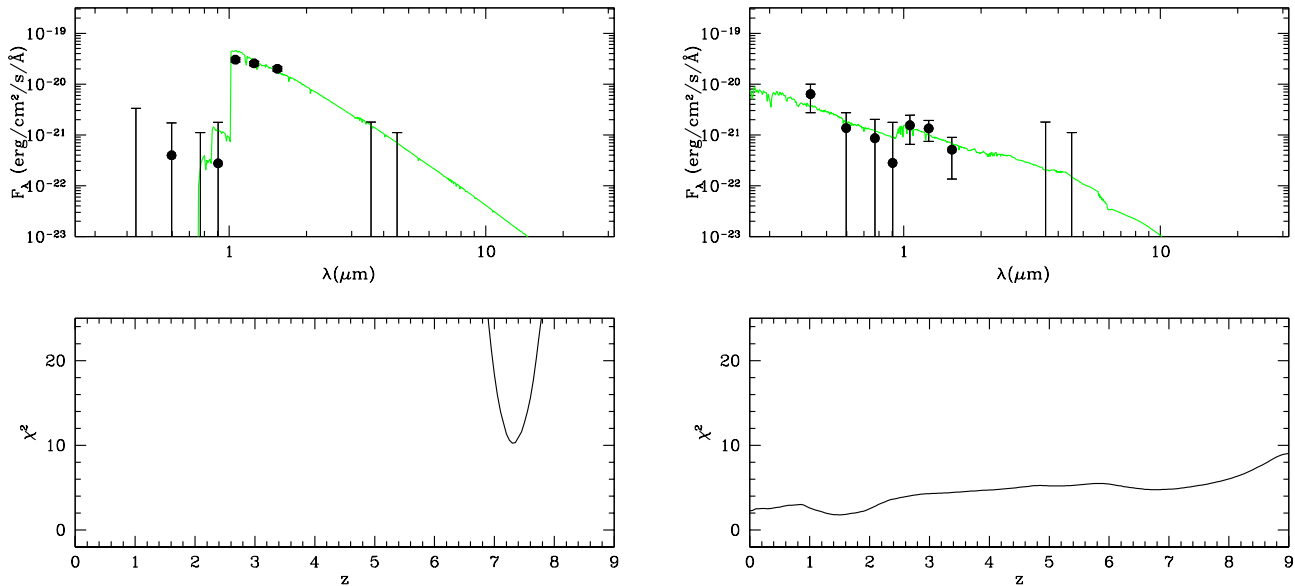


Figure 3. Two different examples of contaminants uncovered within our initial high-redshift galaxy sample. The left-hand plot shows what at first sight appears to be the brightest $z > 7$ galaxy in the sample. However, this is actually a supernova (or some other transient) at RA 03:32:34.53, Dec -27:47:36.0, which has appeared since the original NICMOS F160W imaging of the HUDF. The right-hand plot shows our SED fit to our photometry of UDFz-38537519, the faintest $z \approx 7$ galaxy reported by Oesch et al. (2009b). This in fact appears to be a blue, low-mass galaxy at $z \approx 1.5$, and highlights the problems that can arise when the WFC3/IR data is pushed to a depth at which little colour discrimination can be provided by the ACS optical imaging.

to the boundaries of colour-colour selection boxes in the presence of substantial photometric scatter.

The final outcome of this screening process was a reduction in the number of credible high-redshift ($z \gtrsim 5.9$) galaxy candidates from ≈ 300 to our final catalogue of 49 objects. Before moving on to discuss the properties of our final high-redshift galaxy sample in detail, it is worth commenting on the potential for contamination by ultra-cool galactic T dwarf stars. Due to deep absorption bands in their spectra, galactic T dwarf stars are capable of mimicking the optical–near-infrared colours of $z \approx 7$ galaxies, and consequently, have provided a serious source of contamination for previous ground-based studies in particular. However, due to the combination of image depth, small field of view and high angular resolution (many of our high-redshift candidates are clearly resolved - see Appendix A), contamination of our sample by T dwarfs is expected to be negligible. This is confirmed by considering that the typical absolute J -band (AB) magnitude of T dwarf stars is $J \approx 19$ (Leggett et al. 2009). At the depth probed by our current sample, a T-dwarf contaminant would thus have to be located at a distance of 0.5 – 1.0 kpc. Given this distance is 2 → 3 times the estimated galaxy thin disk scale-height of ≈ 300 pc (e.g. Reid & Majewski 1993; Pirzkal et al. 2009), it is clear that significant contamination is unlikely. This is not to suggest that dwarf stars cannot be found at such distances as, for example, Stanway et al. (2008) report the discovery of M dwarfs out to distances of ≈ 10 kpc. However, in the context of the present study, the surface density is low, with the integrated surface density over all M dwarf types contained within ≈ 1 kpc amounting to ≈ 0.07 per arcmin². Extrapolating these results to T dwarfs is somewhat uncertain, but a comparable surface density for L and T dwarf stars is supported by the search for such stars in deep fields undertaken by Ryan et al. (2005). The results of this study suggest that the 4-arcmin² field-of-view covered by the

new WFC3/IR data should contain ≤ 0.5 T dwarf stars down to a magnitude limit of $z_{850} = 29$.

4.3 The sample

Details on the final high-redshift sample of 49 galaxies are provided in Tables 2 and 3. The galaxies are ranked in order of increasing redshift, and Table 2 summarises the results of the redshift estimation process, giving primary and secondary redshift solutions, along with 1σ confidence intervals, and the minimum value of χ^2 at each solution. With the number of degrees of freedom involved in the fitting process, a solution with $\chi^2 < 9$ must be regarded as statistically acceptable. Postage stamp images, SED fits, and plots of χ^2 versus z for all 49 galaxies are given in Appendix A, with the galaxy candidates again ranked in the same order of increasing primary redshift. Galaxies which have been independently discovered as z_{850} -drops by Oesch et al. (2009b) are marked with a superscript z , while the 5 candidates independently discovered as Y_{105} -drops by Bouwens et al. (2009) are marked with the superscript y .

Table 3 gives the z_{850} , Y_{105} , J_{125} and H_{160} magnitudes for each galaxy, as measured through a 0.6-arcsec diameter aperture, with the WFC3/IR values decreased (i.e. brightened) by the small systematic relative correction factors given above in Section 4.1.

Although we are primarily interested in galaxies at $z > 6.5$ we have retained all galaxy candidates from our original sample which have a primary redshift solution $z > 5.9$, because the redshift probability distributions for these objects frequently extend well beyond $z \approx 6$, and this information requires to be factored into our determination of the galaxy luminosity function at $z \approx 7$. Our insistence on 2σ non-detections in the i -band means that the sample cannot be regarded as reasonably complete until $z > 6.25$. At higher redshifts this sample can be regarded as a master list of

ID	RA(J2000)	Dec(J2000)	z	δz	χ^2	z_2	δz_2	χ_2^2
1735 ⁱ	03 32 39.86	-27 46 19.1	5.90	(5.70-6.05)	6.79	1.20	(1.05-1.30)	14.64
1955 ⁱ	03 32 39.46	-27 45 43.4	5.90	(5.75-6.10)	2.78	1.15	(1.05-1.30)	12.70
1719 ⁱ	03 32 44.70	-27 46 45.6	5.95	(5.75-6.15)	0.77	1.15	(1.05-1.30)	10.94
2217	03 32 40.56	-27 48 02.7	5.95	(5.40-6.20)	2.69	1.20	(1.05-1.40)	5.67
962 ⁱ	03 32 35.05	-27 47 40.1	5.95	(5.80-6.20)	3.54	1.25	(1.15-1.35)	15.55
1189 ⁱ	03 32 36.98	-27 45 57.6	6.00	(5.85-6.15)	1.70	1.20	(1.10-1.30)	16.58
2830	03 32 34.58	-27 46 58.0	6.00	(5.45-6.35)	0.57	1.20	(1.00-1.40)	2.28
2498	03 32 35.04	-27 47 25.8	6.00	(5.70-6.35)	2.47	1.15	(0.95-1.35)	7.81
2719	03 32 40.59	-27 45 56.9	6.05	(5.30-6.90)	0.65	1.25	(1.00-1.60)	2.29
1625 ⁱ	03 32 43.03	-27 46 23.8	6.05	(5.90-6.25)	1.13	1.20	(1.10-1.30)	14.78
1398 ⁱ	03 32 36.63	-27 47 50.1	6.10	(5.90-6.30)	0.46	1.25	(1.10-1.35)	12.87
1760	03 32 40.25	-27 46 05.2	6.15	(5.85-6.45)	0.24	1.25	(1.05-1.40)	6.10
934 ⁱ	03 32 37.48	-27 46 32.5	6.20	(6.00-6.40)	0.58	1.25	(1.15-1.35)	14.82
2791	03 32 36.64	-27 47 50.2	6.25	(5.95-6.50)	1.24	1.25	(1.10-1.40)	8.09
1464	03 32 42.19	-27 46 27.9	6.30	(5.95-6.75)	0.55	1.30	(1.15-1.45)	7.33
2003	03 32 36.46	-27 47 32.4	6.30	(5.65-6.80)	1.39	1.30	(1.00-1.55)	1.67
2514	03 32 39.79	-27 46 33.8	6.30	(5.85-6.75)	0.09	1.25	(0.95-1.50)	3.86
837 ⁱ	03 32 37.46	-27 46 32.8	6.35	(6.15-6.55)	1.18	1.30	(1.20-1.40)	25.79
1855	03 32 43.79	-27 46 33.8	6.40	(6.15-6.70)	0.41	1.30	(1.10-1.45)	7.39
1864	03 32 34.52	-27 47 34.8	6.40	(5.90-6.85)	0.17	1.30	(1.10-1.50)	4.33
1911 ^z	03 32 36.77	-27 47 53.6	6.40	(6.20-6.60)	0.97	1.30	(1.15-1.40)	13.99
1915 ^z	03 32 39.58	-27 46 56.5	6.40	(6.15-6.65)	3.27	1.30	(1.15-1.45)	10.31
2195	03 32 43.05	-27 47 08.1	6.45	(4.75-7.50)	2.39	1.40	(0.00-7.65)	2.63
1880 ^z	03 32 37.44	-27 46 51.3	6.50	(6.25-6.80)	0.36	1.30	(1.15-1.50)	7.77
1958 ^z	03 32 36.38	-27 47 16.2	6.50	(6.25-6.80)	0.17	1.30	(1.15-1.50)	6.93
2206 ^z	03 32 40.58	-27 46 43.6	6.50	(6.20-6.85)	0.83	1.30	(1.15-1.55)	5.03
1064	03 32 34.93	-27 47 01.3	6.65	(6.35-6.90)	2.04	1.35	(1.25-1.50)	14.21
688 ^z	03 32 42.56	-27 46 56.6	6.70	(6.50-6.90)	0.88	1.40	(1.30-1.50)	40.82
2794	03 32 36.75	-27 46 48.2	6.75	(6.20-7.45)	1.37	1.50	(1.20-1.70)	2.45
1144 ^z	03 32 42.56	-27 47 31.5	6.80	(6.50-7.10)	0.40	1.40	(1.25-1.55)	12.94
2395	03 32 44.31	-27 46 45.2	6.80	(6.40-7.30)	1.55	1.45	(1.20-1.65)	4.54
1092 ^z	03 32 39.55	-27 47 17.5	6.85	(6.45-7.35)	3.16	1.55	(1.35-1.75)	8.83
2560 ^z	03 32 37.80	-27 47 40.4	6.90	(6.35-7.45)	0.52	1.45	(1.10-1.75)	3.38
2826	03 32 37.06	-27 48 15.2	6.90	(6.30-7.30)	2.56	1.50	(1.05-1.70)	4.90
1678 ^z	03 32 43.14	-27 46 28.6	7.05	(6.60-7.40)	1.55	1.50	(1.30-1.70)	6.86
2502 ^z	03 32 39.73	-27 46 21.4	7.10	(6.60-7.65)	1.85	1.50	(1.20-1.85)	6.40
1574 ^z	03 32 37.21	-27 48 06.1	7.20	(6.55-7.60)	0.27	1.50	(1.25-1.75)	4.46
835 ^z	03 32 38.81	-27 47 07.2	7.20	(6.90-7.50)	0.90	1.60	(1.45-1.75)	15.99
2066 ^z	03 32 41.05	-27 47 15.6	7.20	(6.50-7.80)	0.60	1.50	(1.15-1.80)	3.69
2888	03 32 44.75	-27 46 45.1	7.35	(6.10-8.35)	0.02	1.60	(0.80-2.10)	0.88
2940	03 32 36.52	-27 46 41.9	7.40	(6.40-8.25)	0.41	1.50	(0.90-2.00)	1.85
2079 ^y	03 32 37.63	-27 46 01.5	7.50	(6.35-8.25)	0.67	1.65	(1.10-2.05)	1.47
1107 ^z	03 32 44.71	-27 46 44.4	7.60	(7.30-7.90)	0.17	1.65	(1.45-1.85)	11.01
1422	03 32 39.52	-27 47 17.3	7.60	(7.00-8.05)	0.17	1.75	(1.45-2.00)	3.52
2487	03 32 33.13	-27 46 54.4	7.80	(7.10-8.30)	1.12	1.75	(1.15-2.00)	3.45
1765 ^y	03 32 42.88	-27 46 34.6	7.95	(7.35-8.50)	1.04	1.90	(1.50-2.05)	2.83
2841 ^y	03 32 43.09	-27 46 27.9	8.10	(7.40-8.75)	1.11	1.90	(1.25-2.20)	2.09
1939 ^y	03 32 37.80	-27 46 00.1	8.35	(7.90-8.70)	3.79	1.90	(1.70-2.15)	4.79
1721 ^y	03 32 38.14	-27 45 54.0	8.45	(7.75-8.85)	0.02	1.95	(1.60-2.15)	2.97

Table 2. Our 49 high-redshift galaxy candidates, ranked in order of increasing primary photometric redshift. Column 1 gives our catalogue number, and a i , z or y superscript is used to indicate objects which have been independently selected as i -drops, z -drops or Y -drops by Bunker et al. (2004), Oesch et al. (2009b) and Bouwens et al. (2009) respectively. Object positions are given in columns 2 and 3. The primary redshift is listed in column 4, with the $1-\sigma$ confidence interval given in column 5, and the minimum χ^2 achieved given in column 6. Columns 7, 8 and 9 give the equivalent information for the secondary redshift solution (see Appendix A for plots of χ^2 versus redshift for each object). We have removed all obvious blended sources from the SExtractor catalogue, but note here that we have retained 934 & 837 as separate objects, and 1422 & 1092 as separate objects, even though in both cases the object pairs are separated by $\simeq 0.5$ arcsec, and the redshift solutions are consistent.

all convincing candidates for galaxies at $z > 6.25$, brighter than a magnitude $\simeq 29$ (AB), in at least one near-infrared passband in the 4.5 arcmin^2 area covered by the WFC3/IR image of the HUDF. It does *not* follow that all candidates are equally robust, as can be judged from the plots presented in Appendix A, and the alternative redshift solutions quantified in Table 2.

Our independent list, selected without recourse to hard optical-infrared colour criteria, contains all but the faintest of the 16 $z \sim 7$ galaxies listed by Oesch et al. (2009b) (which in turn includes the 4 credible $z > 6$ galaxies from Bouwens et al. (2004) listed in Table 1). Our sample also includes all 5 of the $z \sim 8$ galaxies listed by Bouwens et al. (2009).

ID	RA(J2000)	Dec(J2000)	z_{850}	Y_{105}	J_{125}	H_{160}
1735 ⁱ	03 32 39.86	-27 46 19.1	27.81 ± 0.21	28.17 ± 0.22	28.00 ± 0.18	28.14 ± 0.20
1955 ⁱ	03 32 39.46	-27 45 43.4	27.90 ± 0.22	28.28 ± 0.24	28.10 ± 0.19	28.22 ± 0.21
1719 ⁱ	03 32 44.70	-27 46 45.6	28.14 ± 0.27	28.08 ± 0.21	28.09 ± 0.19	28.48 ± 0.26
2217	03 32 40.56	-27 48 02.7	28.54 ± 0.36	28.67 ± 0.32	28.18 ± 0.21	28.40 ± 0.24
962 ⁱ	03 32 35.05	-27 47 40.1	27.90 ± 0.22	27.69 ± 0.16	27.25 ± 0.12	27.33 ± 0.12
1189 ⁱ	03 32 36.98	-27 45 57.6	27.72 ± 0.20	27.70 ± 0.16	27.59 ± 0.14	27.58 ± 0.14
2830	03 32 34.58	-27 46 58.0	28.77 ± 0.44	28.69 ± 0.32	28.80 ± 0.32	28.73 ± 0.31
2498	03 32 35.04	-27 47 25.8	28.81 ± 0.45	28.27 ± 0.24	29.00 ± 0.38	29.12 ± 0.42
2719	03 32 40.59	-27 45 56.9	29.24 ± 0.65	29.07 ± 0.44	28.75 ± 0.31	29.00 ± 0.39
1625 ⁱ	03 32 43.03	-27 46 23.8	27.98 ± 0.24	27.85 ± 0.18	28.08 ± 0.19	28.19 ± 0.21
1398 ⁱ	03 32 36.63	-27 47 50.1	27.96 ± 0.23	27.73 ± 0.16	27.89 ± 0.17	27.91 ± 0.17
1760	03 32 40.25	-27 46 05.2	28.57 ± 0.37	28.25 ± 0.23	28.47 ± 0.25	28.45 ± 0.25
934 ⁱ	03 32 37.48	-27 46 32.5	27.88 ± 0.22	27.30 ± 0.13	27.36 ± 0.12	27.26 ± 0.12
2791	03 32 36.64	-27 47 50.2	28.56 ± 0.37	28.09 ± 0.21	28.36 ± 0.23	28.44 ± 0.25
1464	03 32 42.19	-27 46 27.9	28.72 ± 0.42	28.03 ± 0.20	27.91 ± 0.17	27.90 ± 0.17
2003	03 32 36.46	-27 47 32.4	29.37 ± 0.73	28.50 ± 0.28	28.71 ± 0.30	28.36 ± 0.23
2514	03 32 39.79	-27 46 33.8	29.32 ± 0.69	28.70 ± 0.33	28.91 ± 0.35	29.10 ± 0.42
837 ⁱ	03 32 37.46	-27 46 32.8	28.01 ± 0.24	27.23 ± 0.12	27.24 ± 0.12	27.07 ± 0.11
1855	03 32 43.79	-27 46 33.8	28.84 ± 0.46	28.02 ± 0.20	28.09 ± 0.19	28.30 ± 0.22
1864	03 32 34.52	-27 47 34.8	29.14 ± 0.59	28.37 ± 0.25	28.48 ± 0.26	28.43 ± 0.25
1911 ^z	03 32 36.77	-27 47 53.6	28.61 ± 0.39	27.76 ± 0.17	28.08 ± 0.19	28.15 ± 0.20
1915 ^z	03 32 39.58	-27 46 56.5	29.02 ± 0.54	27.97 ± 0.19	28.20 ± 0.21	28.54 ± 0.27
2195	03 32 43.05	-27 47 08.1	> 29.3	29.27 ± 0.52	30.72 ± 1.66	29.23 ± 0.46
1880 ^z	03 32 37.44	-27 46 51.3	29.20 ± 0.62	28.02 ± 0.20	28.17 ± 0.20	28.36 ± 0.23
1958 ^z	03 32 36.38	-27 47 16.2	29.25 ± 0.65	28.07 ± 0.20	28.26 ± 0.22	28.35 ± 0.23
2206 ^z	03 32 40.58	-27 46 43.6	29.59 ± 0.87	28.35 ± 0.25	28.66 ± 0.29	28.76 ± 0.32
1064	03 32 34.93	-27 47 01.3	28.58 ± 0.37	27.43 ± 0.14	27.35 ± 0.12	27.41 ± 0.13
688 ^z	03 32 42.56	-27 46 56.6	28.14 ± 0.27	26.84 ± 0.10	26.69 ± 0.09	26.68 ± 0.09
2794	03 32 36.75	-27 46 48.2	29.84 ± 1.08	28.59 ± 0.30	28.30 ± 0.22	28.41 ± 0.24
1144 ^z	03 32 42.56	-27 47 31.5	29.29 ± 0.67	27.64 ± 0.15	27.59 ± 0.14	27.53 ± 0.14
2395	03 32 44.31	-27 46 45.2	> 29.3	28.63 ± 0.31	28.36 ± 0.23	28.84 ± 0.34
1092 ^z	03 32 39.55	-27 47 17.5	29.69 ± 0.96	28.05 ± 0.20	27.70 ± 0.15	27.48 ± 0.13
2560 ^z	03 32 37.80	-27 47 40.4	> 29.3	28.86 ± 0.37	28.87 ± 0.34	29.13 ± 0.43
2826	03 32 37.06	-27 48 15.2	> 29.3	28.34 ± 0.25	28.43 ± 0.25	27.89 ± 0.17
1678 ^z	03 32 43.14	-27 46 28.6	> 29.3	28.30 ± 0.24	28.22 ± 0.21	28.08 ± 0.19
2502 ^z	03 32 39.73	-27 46 21.4	> 29.3	28.85 ± 0.37	28.54 ± 0.27	28.95 ± 0.37
1574 ^z	03 32 37.21	-27 48 06.1	> 29.3	28.52 ± 0.28	28.26 ± 0.22	28.13 ± 0.20
835 ^z	03 32 38.81	-27 47 07.2	> 29.3	27.74 ± 0.16	27.28 ± 0.12	27.03 ± 0.10
2066 ^z	03 32 41.05	-27 47 15.6	> 29.3	28.92 ± 0.39	28.40 ± 0.24	28.73 ± 0.31
2888	03 32 44.75	-27 46 45.1	> 29.3	29.57 ± 0.66	28.98 ± 0.37	28.83 ± 0.34
2940	03 32 36.52	-27 46 41.9	> 29.3	29.68 ± 0.73	29.01 ± 0.38	29.51 ± 0.58
2079 ^y	03 32 37.63	-27 46 01.5	> 29.3	29.62 ± 0.69	29.01 ± 0.38	29.33 ± 0.50
1107 ^z	03 32 44.71	-27 46 44.4	> 29.3	28.30 ± 0.24	27.58 ± 0.14	27.70 ± 0.15
1422	03 32 39.52	-27 47 17.3	> 29.3	28.90 ± 0.38	28.07 ± 0.19	27.83 ± 0.16
2487	03 32 33.13	-27 46 54.4	> 29.3	29.73 ± 0.76	28.59 ± 0.28	29.18 ± 0.44
1765 ^y	03 32 42.88	-27 46 34.6	> 29.3	29.44 ± 0.60	28.23 ± 0.21	28.11 ± 0.20
2841 ^y	03 32 43.09	-27 46 27.9	> 29.3	> 30.0	28.98 ± 0.37	29.41 ± 0.54
1939 ^y	03 32 37.80	-27 46 00.1	> 29.3	> 30.0	28.33 ± 0.23	28.49 ± 0.26
1721 ^y	03 32 38.14	-27 45 54.0	> 29.3	> 30.0	28.41 ± 0.24	28.16 ± 0.20

Table 3. Near-infrared photometric information for all 49 galaxies in our high-redshift sample. As a result of our selection criteria, all objects are by definition undetected (at $> 2\sigma$) in the *i*-band, and so here we list the AB magnitudes measured at longer wavelengths, i.e. z_{850} , Y_{105} , J_{125} and H_{160} . All magnitudes were measured through a 0.6-arcsec diameter aperture, with the WFC3/IR values decreased (i.e. brightened) by the small systematic relative correction factors given in Section 4.1. The quoted limits are all 2σ .

Our list contains an additional 15 objects at $z > 6.25$ which have evaded selection by Oesch et al. (2009b) and Bouwens et al. (2009). In general, inspection of the additional objects reveals that they lie just outside or on the edge of the colour selection boxes adopted in these alternative studies. However, use of our own 0.6-arcsec photometry would also lead us to locate several of the objects selected by Oesch et al. and Bouwens et al. outside their adopted selection boxes, and in general the χ^2 plots shown in Ap-

pendix A do not suggest that our additional candidates are any less robust than those selected via strict colour criteria.

In addition to providing a new, more complete list of candidates, our analysis of course yields quantitative constraints on the redshifts of all sources, and information to allow the reader to properly assess the robustness of each individual high-redshift galaxy candidate.

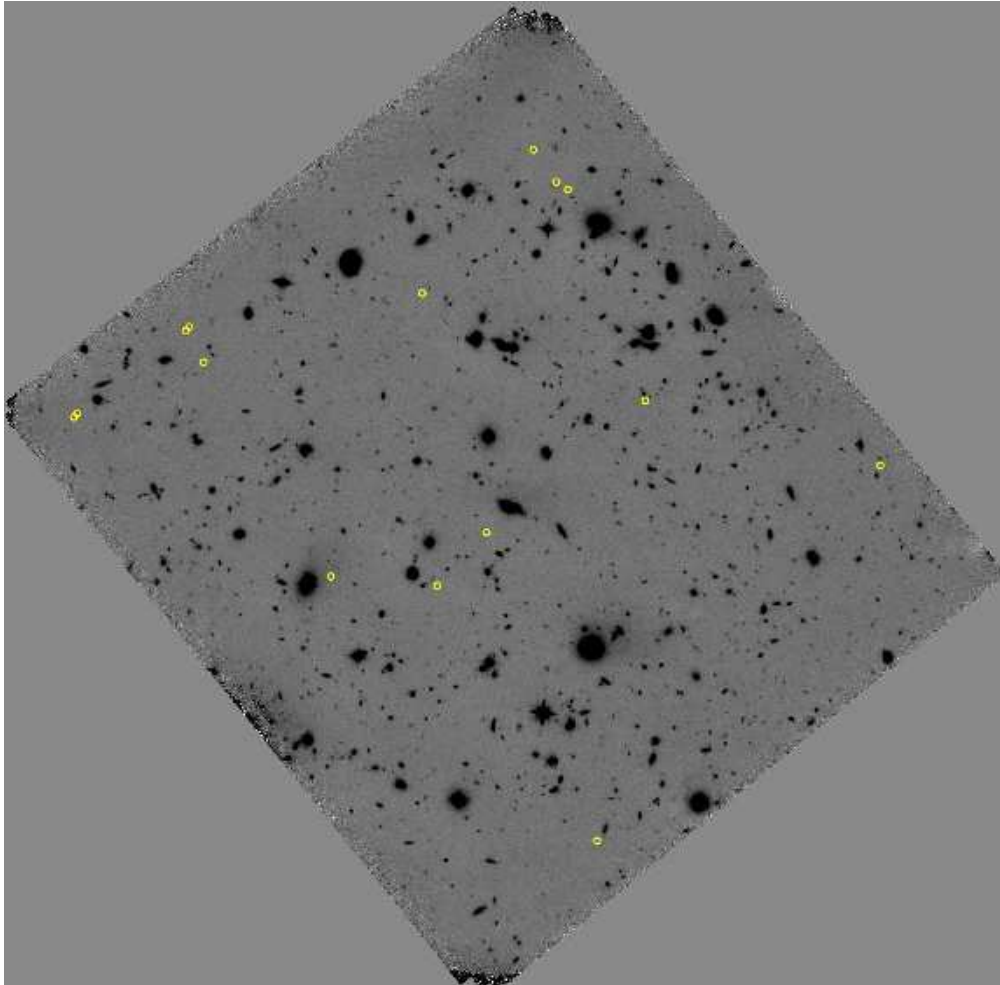


Figure 4. The positions of the 15 galaxies in our sample with primary photometric redshift solutions at $z > 7$ overplotted on the new WFC3/IR H_{160} -band image of the HUDF (North is up, and East is to the left). The 4 most distant galaxies in the sample (at $z > 7.8$) are confined to the groups at the north and north-east of the image.

5 RESULTS

5.1 Galaxies at $z = 7 - 8.5$

Given the natural interest in the possible discovery of galaxies at $z > 7$, we focus first on the existence and robustness of potential galaxies at $z \simeq 8$. As discussed above, our sample contains $\simeq 15$ galaxies at $z > 7$, of which nominally 3 lie at $z > 8$. Of the subsample of 8 galaxies with primary redshift solutions at $z > 7.5$, five are the $z \simeq 8$ galaxy candidates reported by Bouwens et al. (2009), and one was selected as a z -drop by Oesch et al. (2009b). Thus the majority of these apparently extremely distant galaxy candidates have been identified more than once, in independent reductions and analyses of the combined WFC3/IR+ACS dataset. However, we caution that, given the number of degrees of freedom in our SED fitting, any redshift solution with $\chi^2 < 9$ is acceptable at the 2σ level. Thus, given the available data, all 8-10 objects apparently at $z > 7.5$ could also lie at $z \simeq 1.6$, at which point the 4000Å or Balmer break in a galaxy spectrum has begun to move into the F105W bandpass.

The problem here is one of dynamic range. The WFC3/IR imaging is so deep that a non-detection in the ACS z_{850} and other HUDF optical images is not sufficient to discriminate between the extreme Lyman-break at 1215Å anticipated at $z \simeq 8$, from the

more modest 4000Å/Balmer break in a low-luminosity galaxy at much lower redshift. For the faintest proposed $z \sim 8$ galaxy candidates, the available photometry produces redshift constraints which are inevitably rather weak.

Nonetheless, we note here something else of at least qualitative interest about these $z \simeq 8$ galaxy candidates, which is that they appear to be strongly clustered on the sky (see Fig. 4). For example, the four apparently most distant objects in the sample occur in two pairs with projected galaxy separations < 10 arcsec ($\simeq 50$ kpc at $z \simeq 8$). However, it should be cautioned that the suggestion of clustering does not necessarily strengthen the case that these objects are genuine $z \simeq 8$ galaxies, given that the most probable interloper population (i.e. galaxies at $1 < z < 2$) could also be clustered.

Finally, we stress that, even if the high-redshift solutions are adopted for these objects, we have yet to uncover a completely compelling example of a galaxy at $z > 8$ in the WFC3/IR image of the HUDF.

5.2 The ultraviolet galaxy luminosity function at $z = 7 - 8$

Based on our new dataset it is possible to make a preliminary estimate of the ultraviolet (UV) galaxy luminosity function at $z = 7$ and $z = 8$. In order to exploit the redshift information available for

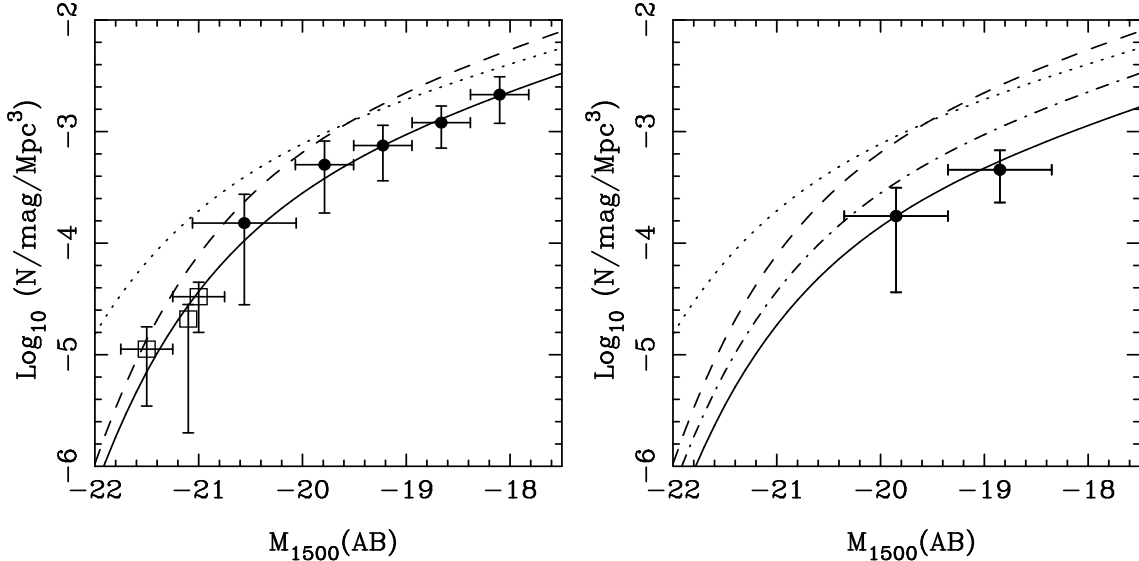


Figure 5. Our new determinations of the ultraviolet (UV) galaxy luminosity function at $z \simeq 7$ and $z \simeq 8$. The left-hand panel shows our V/V_{\max} estimate of the redshift $z = 7$ luminosity function. The absolute UV magnitudes have been calculated at a rest-frame wavelength of 1500\AA . The filled circles are the data-points from this study, where the horizontal error bars indicate the width of the magnitude bins adopted (either $\Delta m = 0.5$ or $\Delta m = 1.0$ depending on signal-to-noise) and the vertical error bars indicate the uncertainty due to simple Poisson statistics. The open squares are taken from the ground-based study of the Subaru Deep Field and GOODS-North field by Ouchi et al. (2009). The dotted and dashed curves are the Schechter function fits to the $z = 5$ and $z = 6$ luminosity function from McLure et al. (2009). The solid line is our best-fitting Schechter function to the $z = 7$ luminosity function. The right-hand panel shows our corresponding estimate of the luminosity function at redshift $z = 8$. In this panel the dashed and dot-dashed curves are the $z = 6$ and $z = 7$ Schechter function fits from McLure et al. (2009) and this work respectively. The solid line is the best-fitting $z = 7$ Schechter function with ϕ^* reduced by a factor of two (see text for a discussion).

our sample, when deriving the luminosity function we adopt the method outlined in McLure et al. (2009) whereby, rather than simply adopting the primary photometric redshift solution, each object is represented by its normalized redshift probability density function. In addition to making better use of the available information, this method makes it possible to construct the luminosity function using the classic V/V_{\max} estimator of Schmidt (1968), and deals with the problem of multiple redshift solutions in a transparent fashion.

In Fig. 5 we show our estimates of the $z = 7$ and $z = 8$ galaxy luminosity functions, which were calculated within the redshift intervals $6.5 < z < 7.5$ and $7.5 < z < 8.5$ respectively. In both panels the data-points from this study are shown as the filled circles, and in the left-hand panel we also plot the $z = 7$ data-points at bright magnitudes from the ground-based study of the Subaru Deep Field and GOODS-North field by Ouchi et al. (2009). Although a full analysis of the evolving UV-selected luminosity function is deferred until the remainder of the deep HUDF09 WFC3/IR data are obtained over the coming year, we have performed a simple fit to the $z = 7$ luminosity function, including the Ouchi et al. (2009) data-points at the bright end. The best-fitting Schechter function is shown as the solid line in the left-hand panel of Fig. 5 and yields the following parameter values: $M_{1500}^* = -20.11$, $\phi^* = 0.0007 \text{Mpc}^{-3}$ and $\alpha = -1.72$. Due to the large uncertainties on the data-points it is not possible to place meaningful constraints on either M_{1500}^* or α at $z = 7$. However, a comparison with the best-fitting Schechter luminosity function parameters at $z = 6$ ($M_{1500}^* = -20.04 \pm 0.12$, $\phi^* = 0.0018 \pm 0.0005 \text{Mpc}^{-3}$ and $\alpha = -1.71 \pm 0.11$) from McLure et al. (2009), suggests that the $z = 6$ and $z = 7$ luminosity functions have very similar shapes, and can be reconciled via an evolution in number density by a factor of $\simeq 2.5$.

The limited dynamical range in absolute luminosity makes it impossible, at present, to place any meaningful constraints on the shape of the UV-selected galaxy luminosity function at $z = 8$. All that can be said with the current dataset is that, at a characteristic luminosity of $M_{1500} \simeq -19.5$, the number density of high-redshift galaxies is a further factor of $\simeq 2$ smaller than at $z = 7$. To illustrate this point we show in the right-hand panel of Fig. 5 that the best-fitting Schechter function at $z = 7$ can be brought into good agreement with the $z = 8$ data-points simply by reducing ϕ^* by a factor of two. Although the uncertainties associated with the current dataset, along with degeneracies between Schechter function parameters, prevent any definitive conclusions, it appears that the $z = 7$ and $z = 8$ luminosity functions are consistent with having the same overall shape as at $z = 6$, but with ϕ^* a factor of $\simeq 2.5$ and $\simeq 5$ lower respectively.

5.3 Implications for re-ionisation

Given the apparent decline in the number density of star-forming galaxies over the redshift range $z \simeq 6 - 8$, it is prudent to examine the ability of the observed population of galaxies to achieve reionisation. We adopt the method of Bolton & Haehnelt (2007), converting the observed luminosity functions at $z > 6$ to ionising emissivities assuming a Salpeter IMF, a metallicity of $0.2 Z_{\odot}$, and an escape fraction for ionising photons of 20%. For simplicity, we ignore any possible mass dependence in the escape fraction. We consider relatively low values for the hydrogen clumping factors in our analysis ($C \simeq 2 - 5$), following the results of recent simulations (e.g. Bolton & Haehnelt 2007). At $z < 6$, we adopt the comoving ionising photon density implied by the Ly α opacity data presented in Bolton & Haehnelt (2007), where $\dot{N}_{ion}(z) = 10^{50.5 - 0.06(z-6)} s^{-1} \text{Mpc}^{-3}$.

For the luminosity function at $z \simeq 7$ and 8 , we adopt the

$z \simeq 6$ Schechter parameters from McLure et al. (2009), with the normalisation (ϕ^*) lowered by a factor of 2.5 and 5, respectively, consistent with the measurements presented above. To provide an upper bound on the possible contribution of the star-forming galaxy population to reionisation, we first assume the luminosity function remains constant over $8 < z < 15$ and compute the evolution of the filling factor of ionised hydrogen, Q_{HII} , as a function of redshift. To do this, we integrate the ionising emissivities forward from $z = 15$, arbitrarily assuming that the ionising flux decreases to zero at $z > 15$. Defining the end of reionisation as the redshift when $Q_{HII} = 1$, we find that if we include only sources brighter than $M = -18$ (roughly the detection limit of the WFC3 data at $z = 7$), the IGM would not achieve a unity HII filling factor until $z = 4.2$, at odds with the high ionisation fraction implied by measurements of the Gunn Peterson optical depth from quasars at $z \lesssim 6.2$ (e.g. Fan et al. 2006, Becker et al. 2007). Even if sources as faint as $M = -10$ are included, reionisation would only be completed at $z = 4.5$ (with $Q_{HII} = 0.53$ at $z = 6.0$), at odds with the transmission seen in quasar spectra at these redshifts. Furthermore, each of these computations assumes that the ionising emissivity does not decrease beyond $z = 8$. If the normalisation of the luminosity function instead continues to decline at $z > 8$, consistent with the trends at $6 < z < 8$, then the galaxy population would undoubtedly be hard-pressed to reionise the IGM by $z \simeq 6$ without significant variations in the escape fraction. While caution must surely be exercised in interpreting these results given the uncertainties in the form of the luminosity functions, our results indicate that it is difficult for the observed population of star-forming galaxies to achieve reionisation by $z \simeq 6$ without a significant contribution from galaxies well below the detection limits, in addition to alterations in the escape fraction of ionising photons and/or continued vigorous star formation at $z > 15$.

6 SUMMARY

Following the first public data release of the raw WFC3/IR data taken within the HUDF (as part of HST Treasury programme GO-11563), we have reduced the new deep Y_{105} , J_{125} , and H_{160} images, and analysed them in tandem with the existing deep optical B , V , i , z ACS imaging, to conduct a new systematic search for high-redshift galaxies at $z = 6 - 9$. After registering the new infrared data to the ACS optical image reference frame, and establishing our own photometric zero-points, we used SExtractor to select a complete parent catalogue consisting of all objects which were detected at $\geq 5\sigma$ significance in at least one of the near-infrared wavebands in a 0.4-arcsec diameter aperture. For the purposes of SED analysis and photometric redshift determination we performed aperture photometry on all objects within circular apertures of 0.6-arcsec diameter, applying relative (to ACS resolution) point-source aperture corrections to the derived Y_{105} , J_{125} , and H_{160} magnitudes.

Starting from the master catalogue we confined our attention to high redshifts by rejecting all sources which were detected at $\geq 2\sigma$ significance in the ACS i -band imaging. We then performed full SED fitting to the optical+infrared photometry of the remaining $\simeq 300$ objects in the catalogue, and utilised this information to inform the rejection of a variety of contaminants (stars, diffraction spikes, transients) and lower-redshift galaxy interlopers. The final result is a sample of 49 galaxies with primary photometric redshift solutions $z > 5.9$, within the 4.5 arcmin² field covered by the new near-infrared imaging. Our sample, selected without re-

course to specific colour cuts, re-selects all but the faintest one of the 16 z_{850} -drops selected by Oesch et al. (2009), recovers all 5 of the Y_{105} -drops reported by Bouwens et al. (2009), and adds a further 29 equally plausible galaxy candidates, of which 12 lie beyond $z \simeq 6.3$, and 4 lie beyond $z \simeq 7.0$. However, we also present confidence intervals on our photometric redshift estimates, marginalising over all other fitted parameters, and highlight the prevalence of alternative secondary redshift solutions (especially for the highest redshift galaxy candidates). As a result of this analysis we caution that acceptable low-redshift ($z < 2$) solutions exist for 28 out of the 37 galaxies at $z > 6.3$, and in particular for all 8 of the galaxy candidates reported here at $z > 7.5$. Nevertheless, we note that the very highest redshift candidates appear to be strongly clustered in the field.

Based on our photometric redshift analysis we derive new estimates of the ultraviolet galaxy luminosity function at $z \simeq 7$ and $z \simeq 8$. Where our results are most robust, at a characteristic luminosity $M_{1500} \simeq -19.5(AB)$, we find that the comoving number density of galaxies declines by a factor of $\simeq 2.5$ between $z \simeq 6$ and $z \simeq 7$, and by a further factor of 2 by $z \simeq 8$. These results suggest that it is difficult for the observed population of high-redshift star-forming galaxies to achieve reionisation without a significant contribution from galaxies well below the detection limits plus alterations in the escape fraction of ionising photons and/or continued vigorous star formation at $z > 15$.

ACKNOWLEDGEMENTS

The authors would like to thank the anonymous referee whose comments and suggestions significantly improved the final version of this manuscript. This work is based primarily on observations made with the NASA/ESA *Hubble Space Telescope*, which is operated by the Association of Universities for Research in Astronomy, Inc, under NASA contract NAS5-26555. This work is based in part on observations made with the *Spitzer Space Telescope*, which is operated by the Jet Propulsion Laboratory, California Institute of Technology under NASA contract 1407. RJM and JSD acknowledge the support of the Royal Society through a University Research Fellowship and a Wolfson Research Merit award respectively. MC and DS acknowledge the support of STFC through the award of an Advanced Fellowship and Post-Doctoral Fellowship respectively. TAT acknowledges the support of NSERC.

REFERENCES

- Becker G.D., Rauch M., Sargent W.L.W., 2007, ApJ, 662, 72
- Beckwith S.V.W., et al., 2006, AJ, 132, 1729
- Bertin E., Arnouts S., 1996, A&AS, 117, 39
- Bolton J.S., Haehnelt M.G., 2007, MNRAS, 382, 325
- Bolzonella M., Miralles J.-M., Pelló R., 2000, A&A, 363, 476
- Bouwens R.J., et al., 2004, ApJ, 616, L79
- Bouwens R.J., Illingworth G.D., Blakeslee J.P., Franx M., 2006, ApJ, 653, 53
- Bouwens R.J., et al., 2008, ApJ, 686, 230
- Bouwens R.J., et al., 2009, ApJ, submitted (arXiv:0909.1803)
- Bradley L.D., et al., 2008, ApJ, 678, 647
- Bunker A.J., Stanway E.R., Ellis R.S., McMahon R.G., 2004, MNRAS, 355, 374
- Calzetti D., et al., 2000, ApJ, 533, 682
- Dunkley J., et al., 2009, ApJ, 180, 306
- Dunlop J.S., Cirasuolo M., McLure R.J., 2007, MNRAS, 376, 1054

- Eyles L.P., Bunker A.J., Ellis R.S., Lacy M., Stanway E.R., Stark D.P., Chue K., 2007, MNRAS, 374, 910
- Fan X., et al., 2006, AJ, 132, 117
- Fazio G.G., et al., 2004, ApJS, 154, 10
- Fruchter A.S., Hook R.N., 2002, PASP 114, 144
- Gunn J.E., Peterson B.A., 1965, ApJ, 142, 1633
- Iye M., et al., 2006, Nature, 443, 186
- Koekemoer A., et al., 2002, HST Calib. Workshop, 337
- Labbé I., Bouwens R., Illingworth G.D., Franx M., 2006, ApJ, 649, L67
- Labbé I., et al., 2009, ApJ, submitted, arXiv0910.0838
- Leggett S.K., et al., 2009, ApJ, 695, 1517
- Madau P., 1995, ApJ, 441, 18
- McLure R.J., Cirasuolo M., Dunlop J.S., Foucaud S., Almaini O., 2009, MNRAS, 395, 2196
- Oesch P.A., et al., 2007, ApJ, 671, 1212
- Oesch P.A., et al., 2009a, ApJ, 690, 1350
- Oesch P.A., et al., 2009b, ApJ, submitted (arXiv:0909.1806)
- Oke J.B., Gunn J.E., 1983, ApJ, 266, 713
- Ouchi M., et al., 2009, ApJ, submitted (arXiv:0908.3191)
- Pirzkal N., et al., 2009, ApJ, 695, 1591
- Reid N., Majewski S.R., 1993, ApJ, 409, 635
- Richard J., et al., 2008, ApJ, 685, 705
- Ryan R.E., et al., 2005, ApJ, 631, L159
- Salvaterra R., et al., 2009, Nature, submitted (arXiv:0906.1578)
- Stanway E.R., Bremer M.N., Lehnert M.D., Eldridge J.J., 2008, MNRAS, 384, 348
- Shapley A. E., Steidel C. C., Pettini M., Adelberger K. L., 2003, ApJ, 588, 65
- Stark D.P., Ellis R.J., Richard J., Kneib J.-P., Smith G.P., Santos M.R., 2007, ApJ, 663, 10
- Stark D.P., Ellis R.J., Bunker A., Bundy K., Targett T., Benson A., Lacy M., 2009, ApJ, 697, 1493
- Steidel C.C., Giavalisco M., Pettini M., Dickinson M., Adelberger K.L., 1996, ApJ, 462, 17
- Szalay A.S., Connolly A.J., Szokoly G.P., 1999, AJ, 117, 68
- Tanvir N.R., et al., 2009, Nature, submitted (arXiv:0906.1577)
- Thompson R.I., et al., 2005, AJ, 130, 1
- Yan H., Windhorst R.A., 2004, ApJ, 612, L93
- Zheng W., et al., 2009, ApJ, 697, 1907

APPENDIX A: SED FITS AND REDSHIFT ESTIMATES

In this appendix we present detailed information on each of our 49 high-redshift galaxy candidates, to facilitate comparison with other studies and to allow the reader to judge for themselves the robustness of the high-redshift solutions. The galaxies are ranked in order of increasing primary redshift. For each galaxy we provide optical and near-infrared postage stamp grey-scale images, and also a plot showing the best fitting galaxy SED, and the dependence of χ^2 on redshift (marginalised over all other fitted parameters).

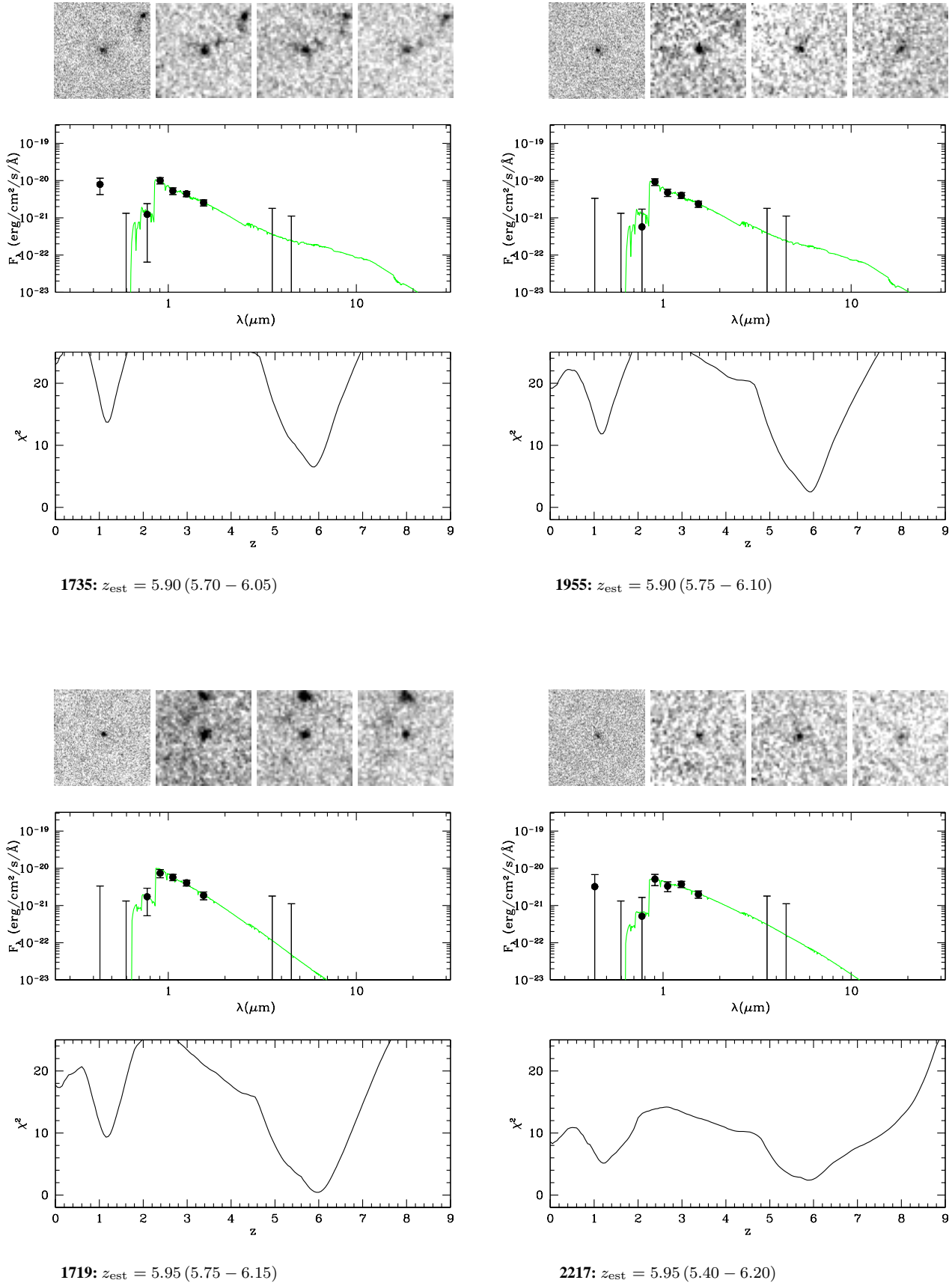


Figure A1. 3×3 arcsec z_{850} , Y_{105} , J_{125} , H_{160} (left to right) greyscale ($-2\sigma - +6\sigma$) postage-stamp images are shown for each galaxy candidate above a plot which shows the galaxy SED which best fits the HST ACS optical, WFC3/IR near-infrared and Spitzer 3.6 μm and 4.5 μm photometric limits. The lower panel for each object shows how χ^2 varies with redshift, marginalised over galaxy age, star-formation history, and dust reddening. The ID number of each source, and its estimated redshift (with 1σ error range) are given under each plot.

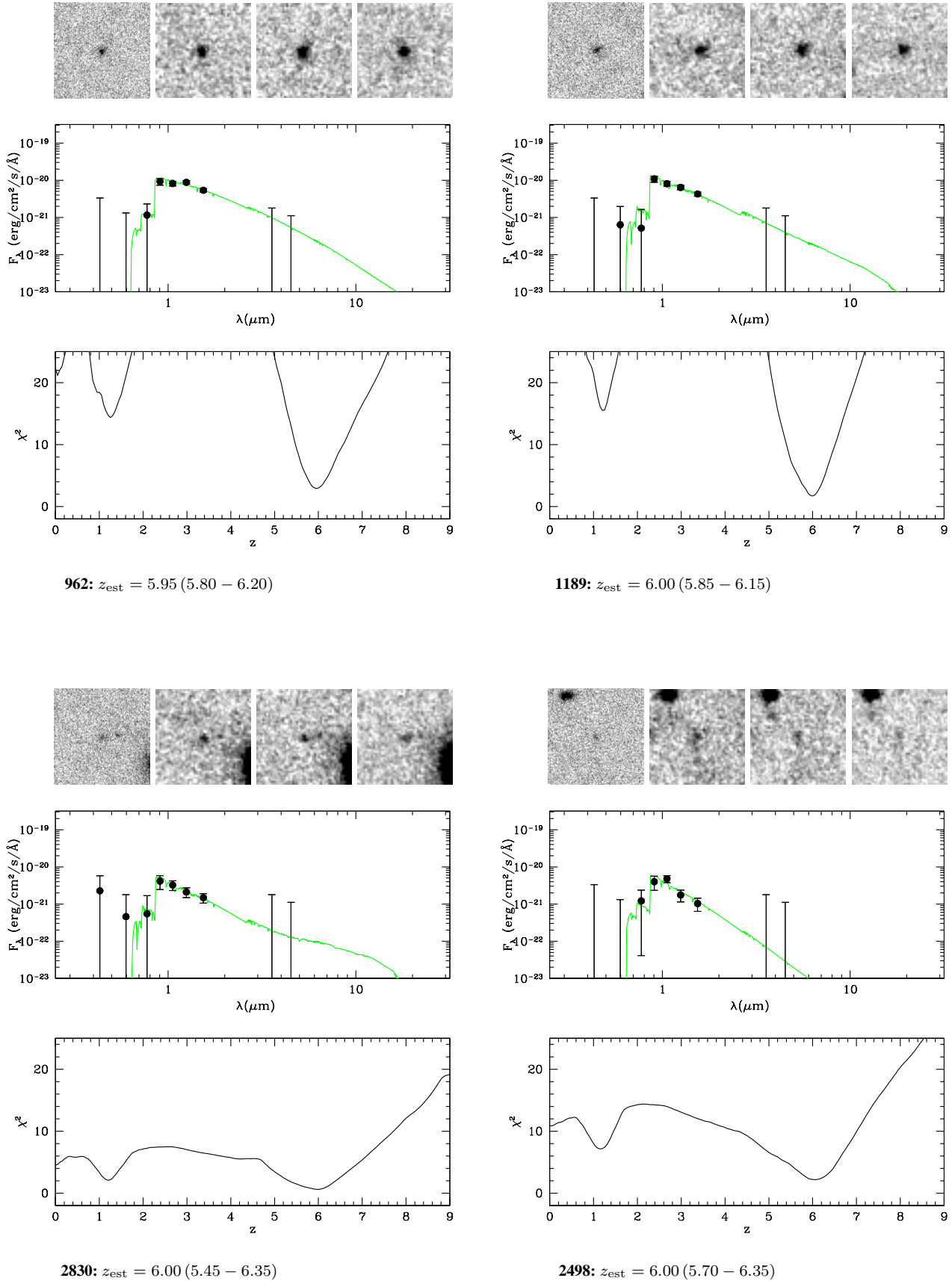


Figure A1. continued.

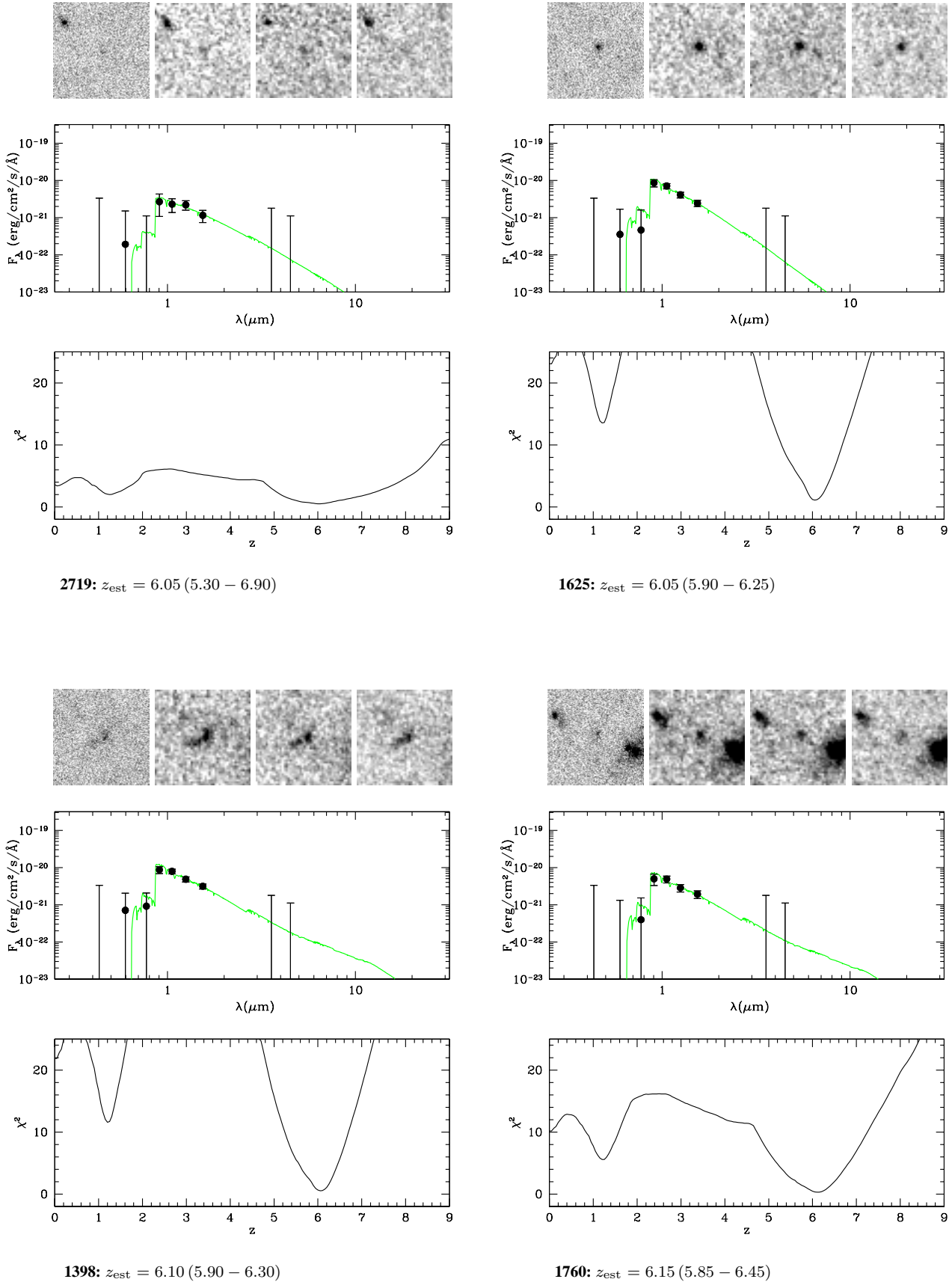


Figure A1. continued.

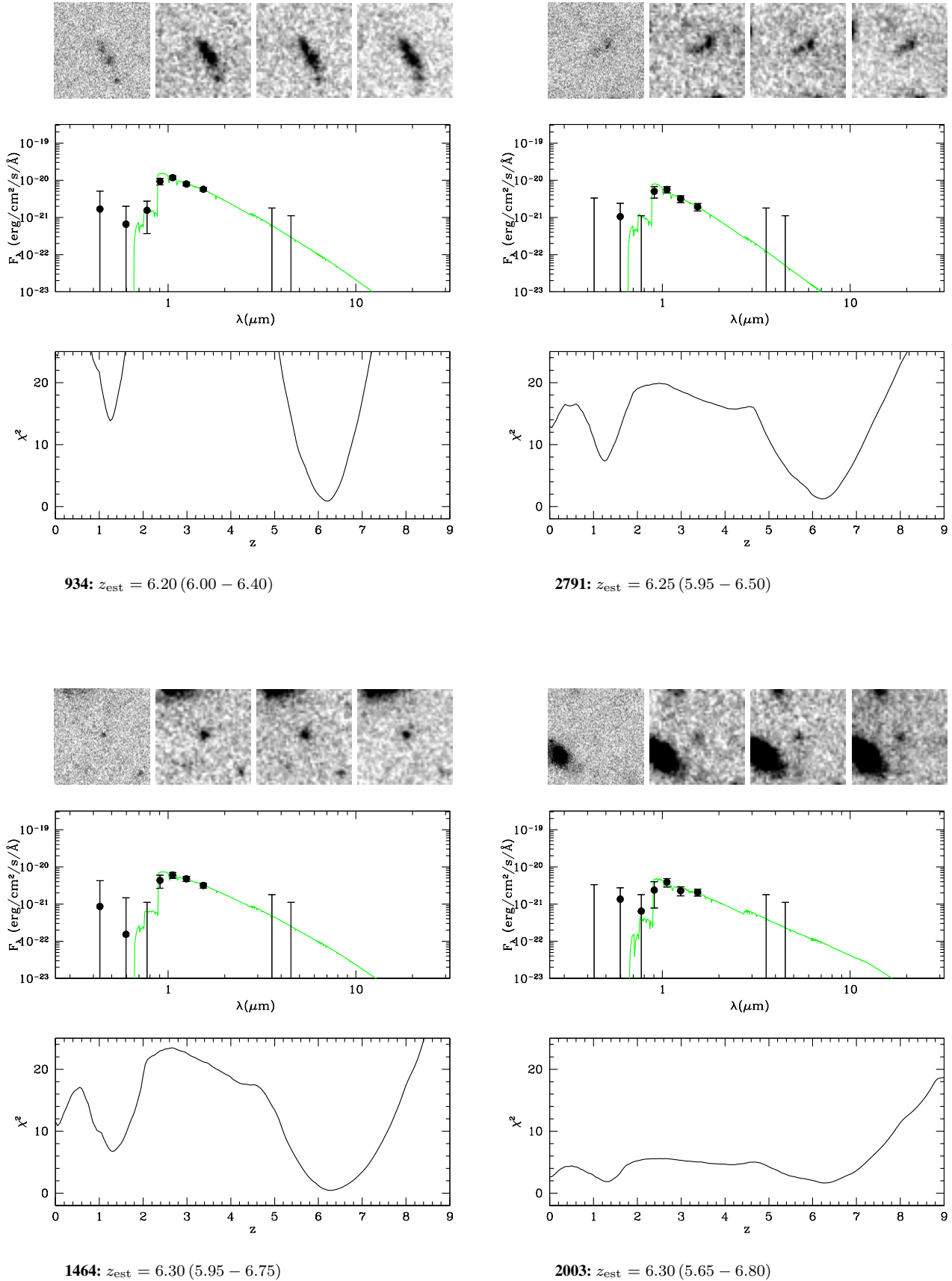


Figure A1. continued.

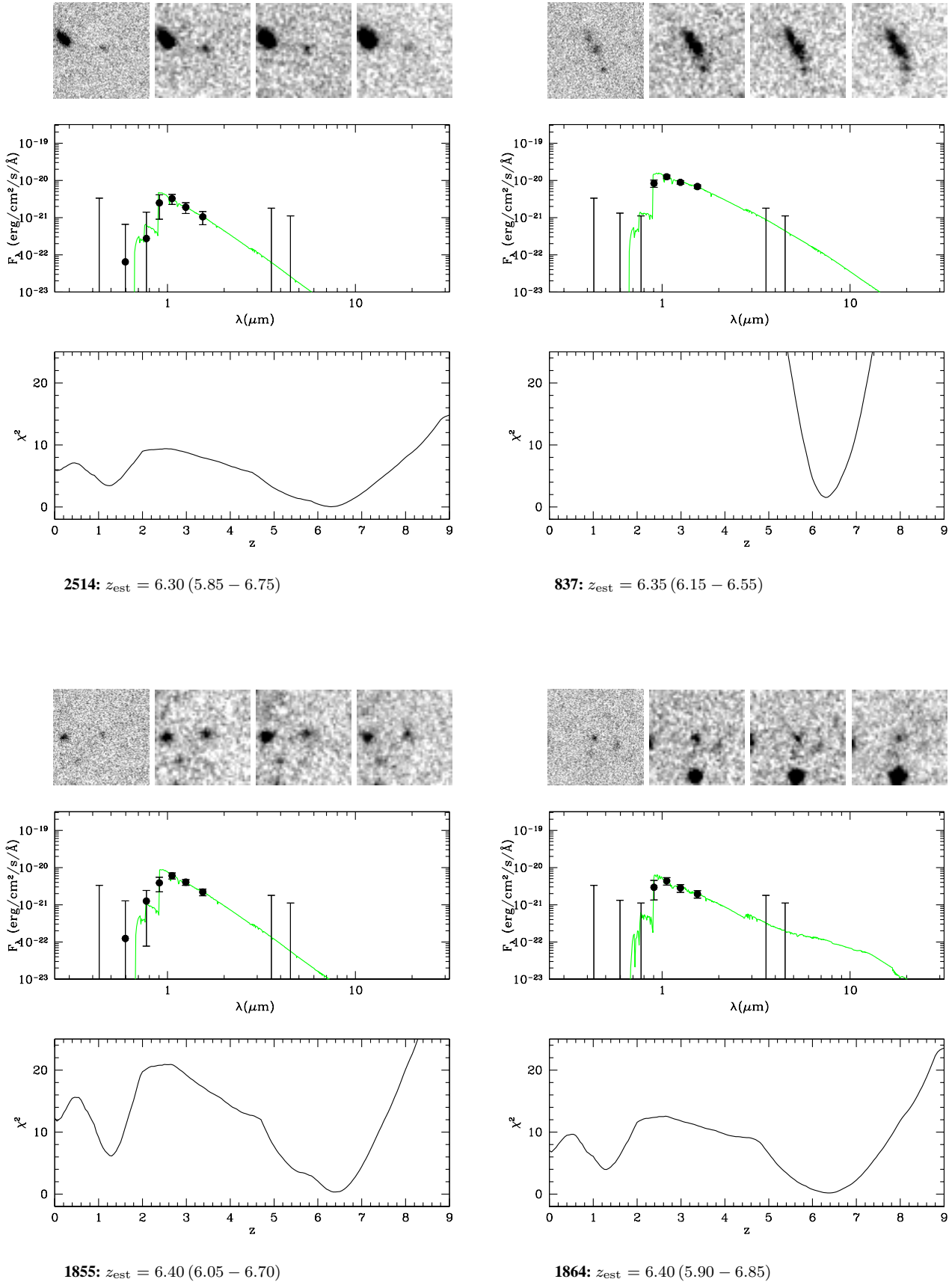


Figure A1. continued.

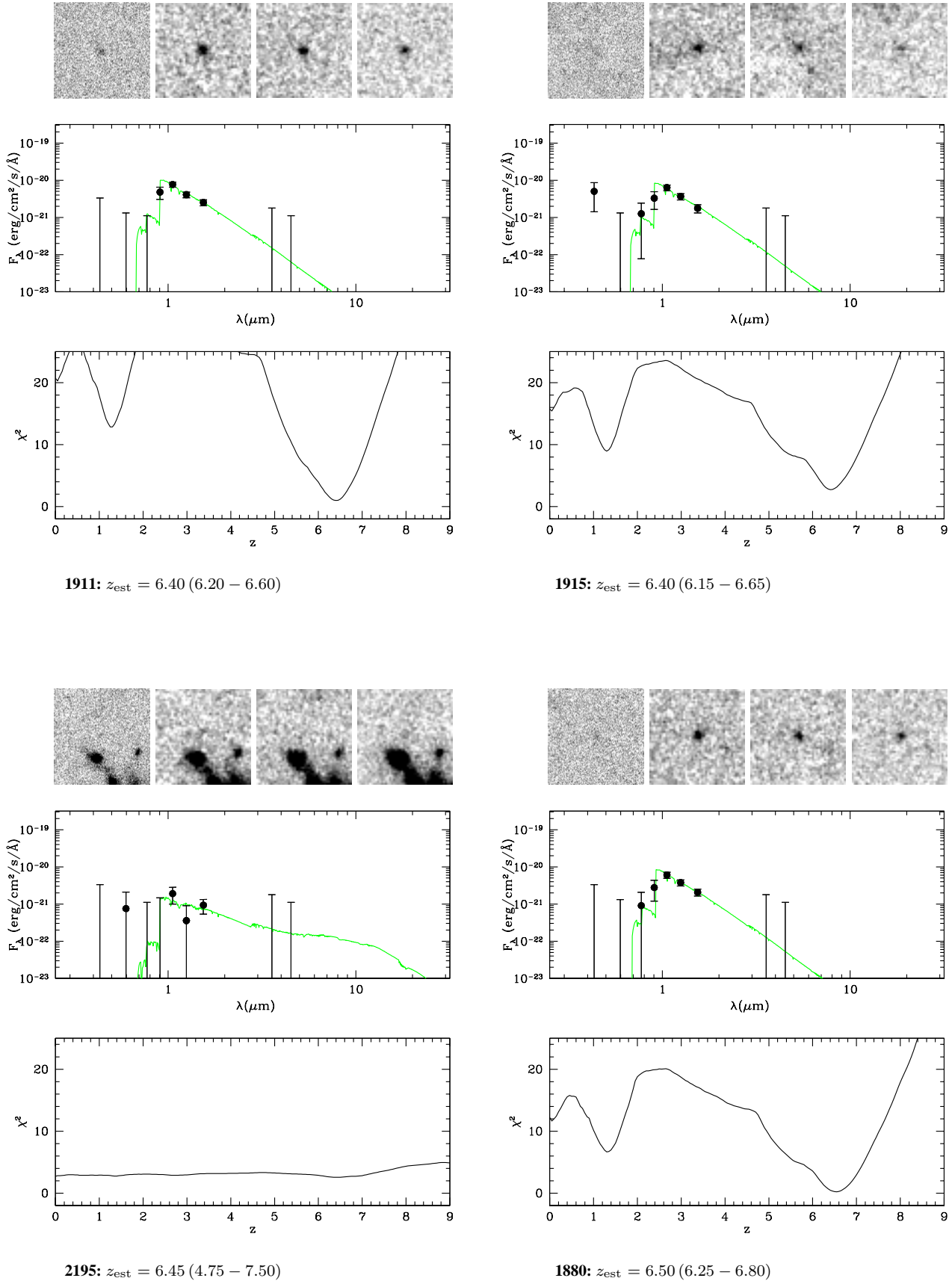


Figure A1. continued.

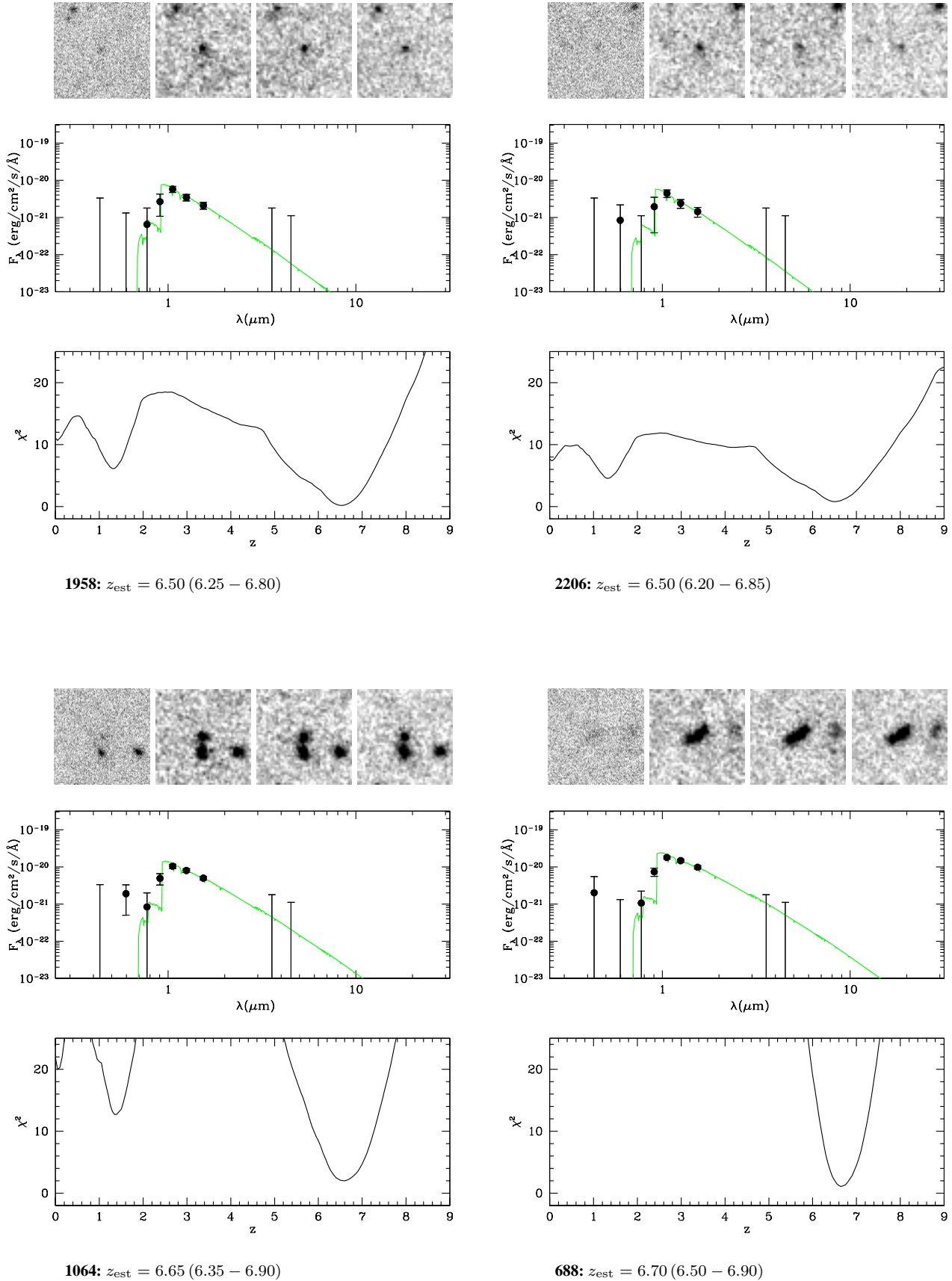


Figure A1. continued.

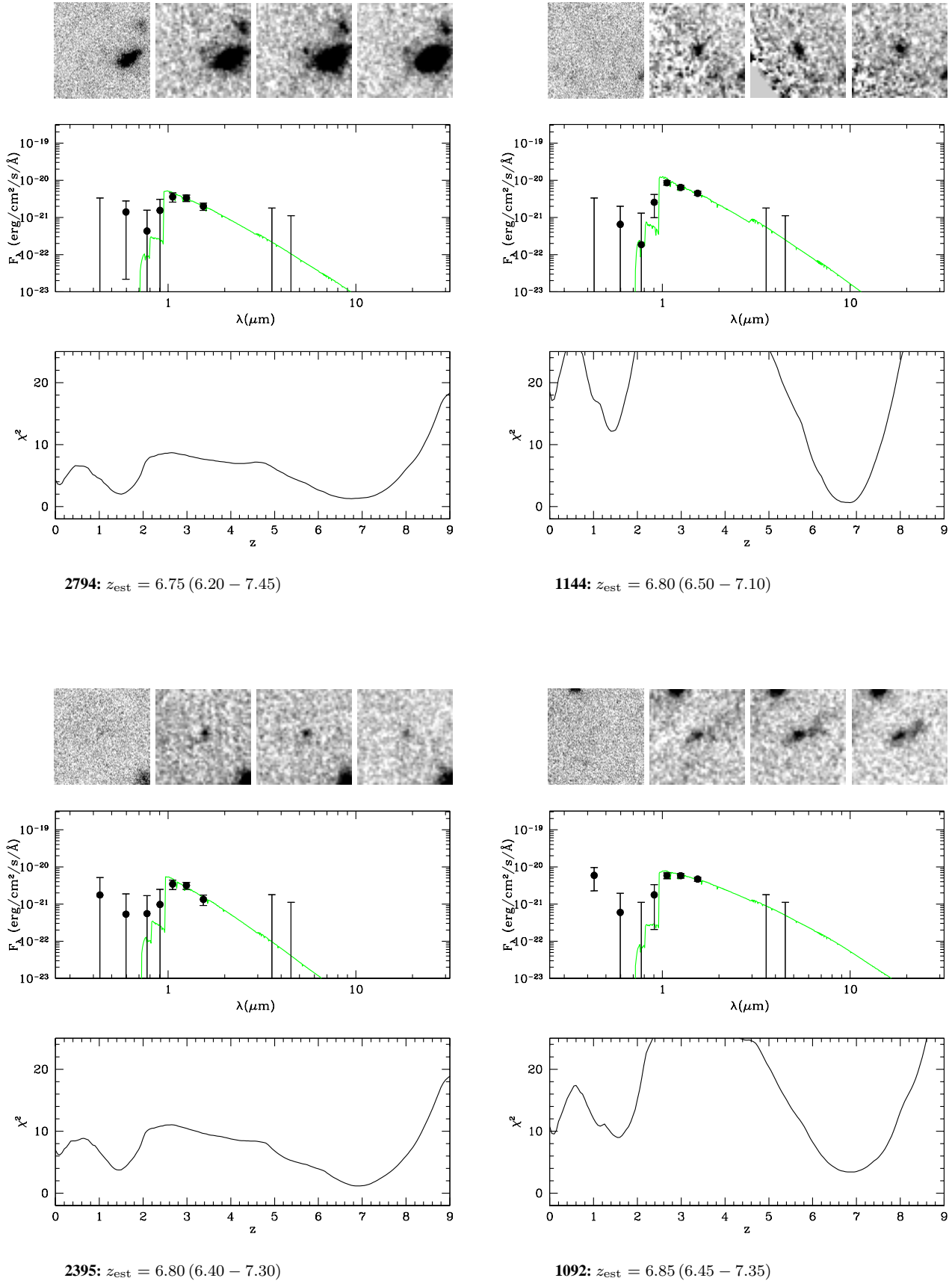


Figure A1. continued.

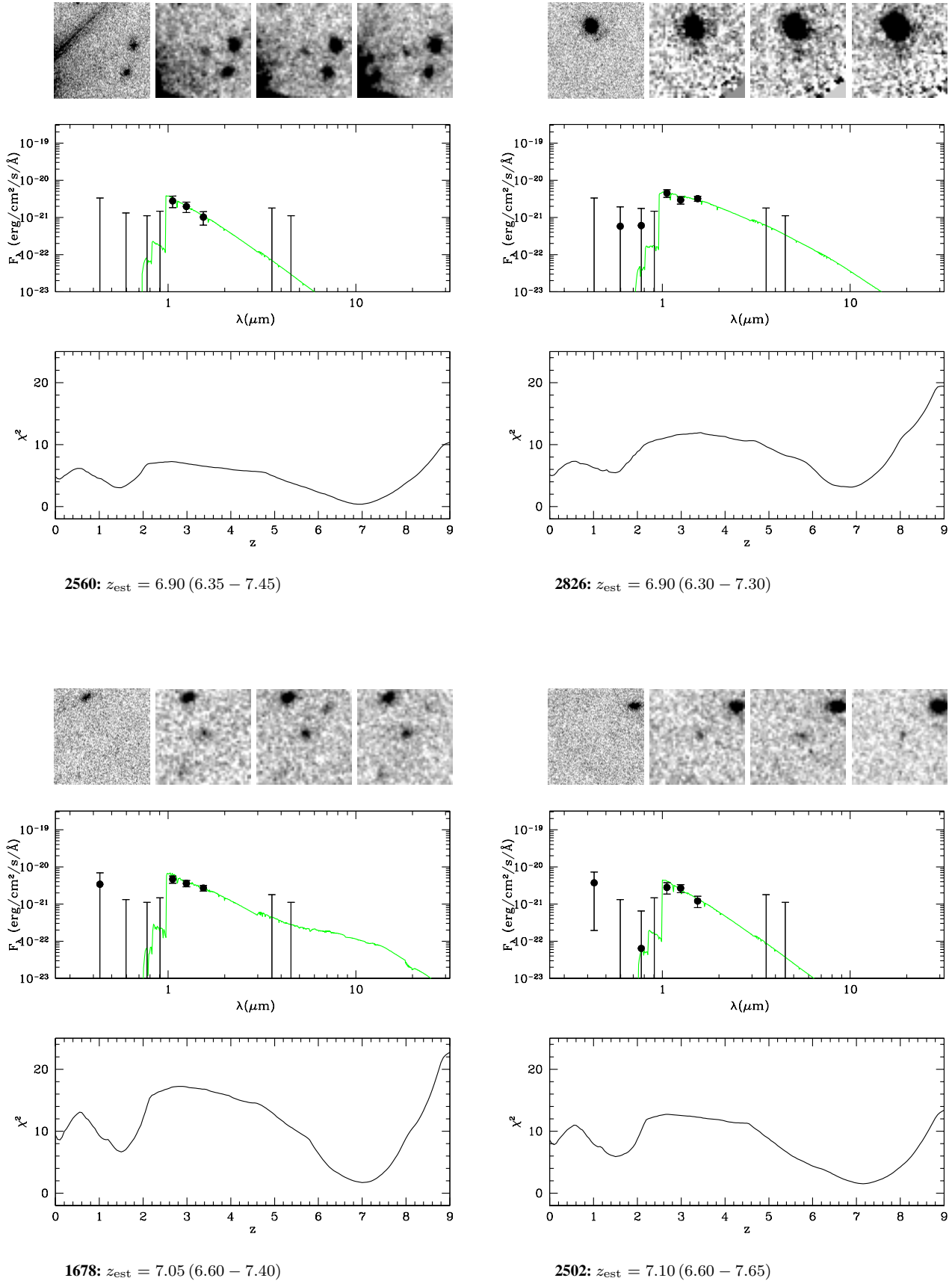


Figure A1. continued.

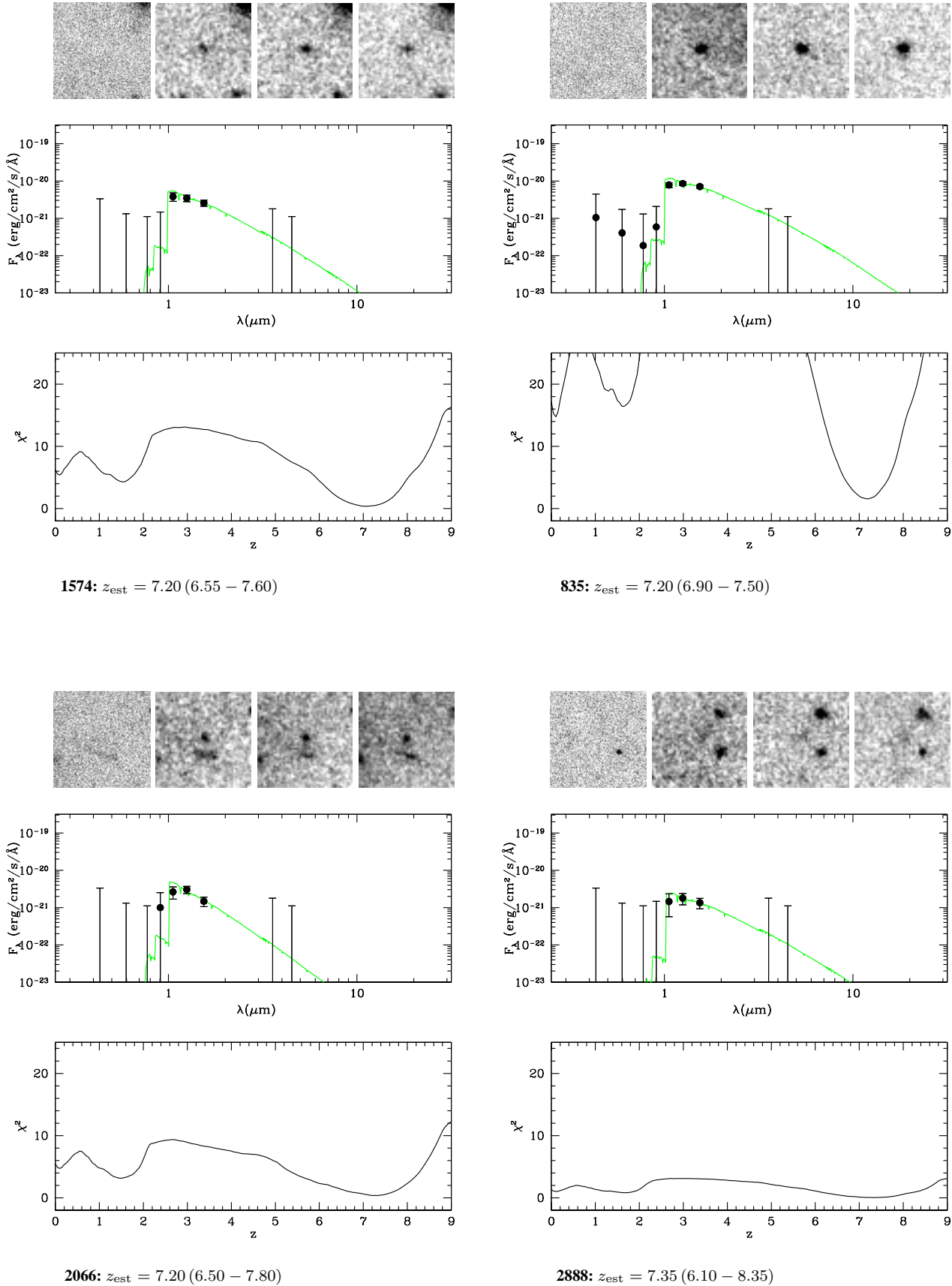


Figure A1. continued.

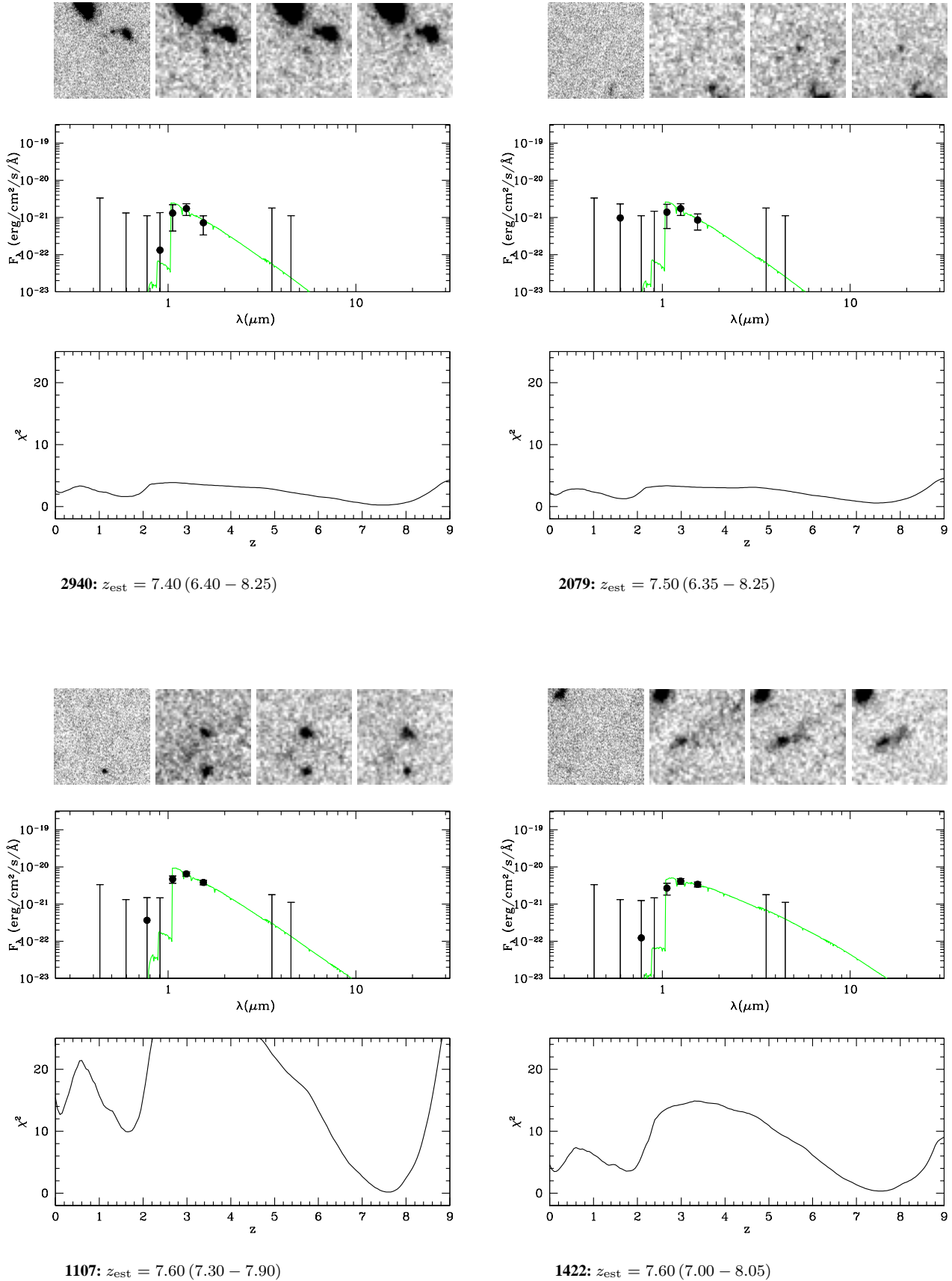


Figure A1. continued.

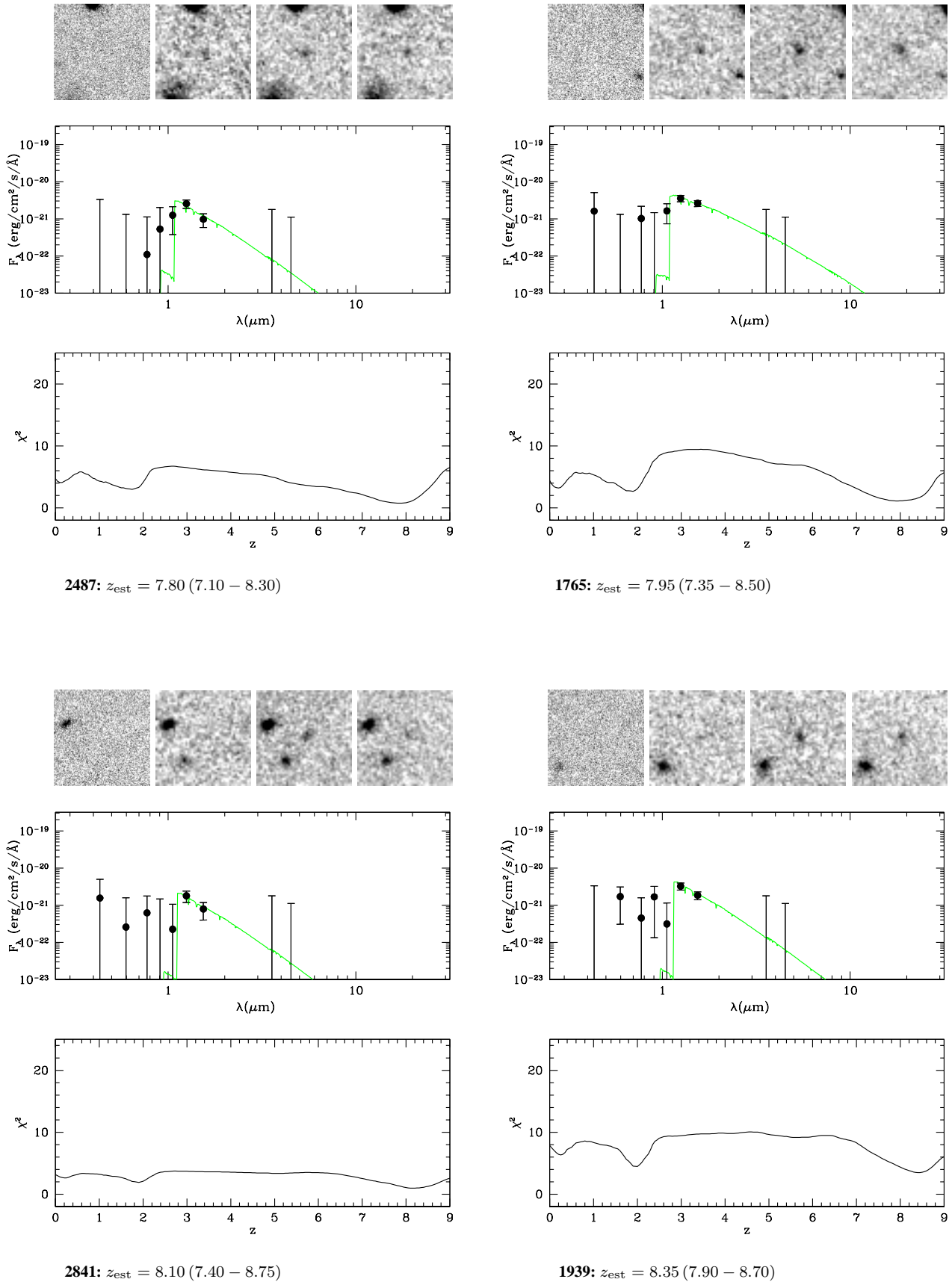


Figure A1. continued.

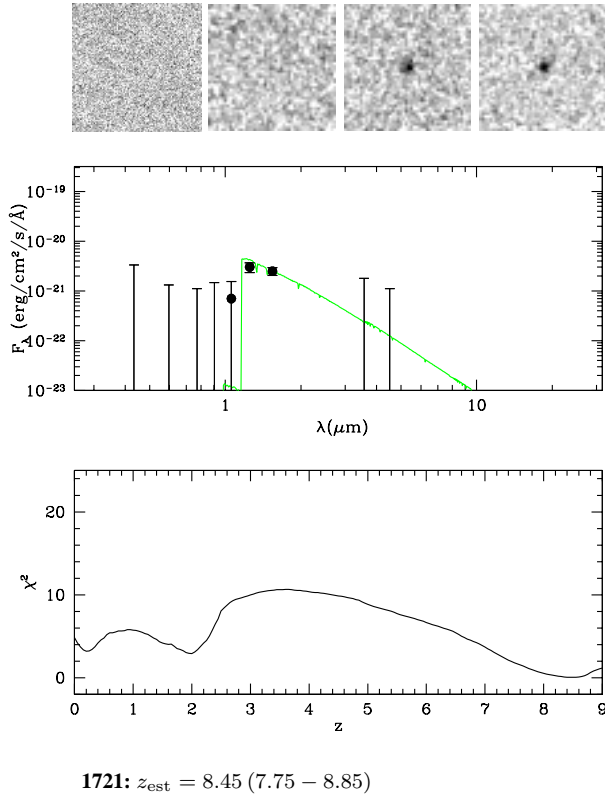


Figure A1. continued.